STUDY AND APPLICATIONS OF LIQUID BEHAVIOR ON MICROTEXTURED SOLID SURFACES

BY

TARUN MALIK

DISSERTATION

Submitted in partial fulfillment of the requirements
for the degree of Doctor of Philosophy in Mechanical Engineering
in the Graduate College of the
University of Illinois at Urbana-Champaign, 2011

Urbana, Illinois

Doctoral Committee:

Assistant Professor Nicholas X. Fang, Chair
Professor Anthony M. Jacobi
Professor Paul J. A. Kenis
Professor Taher A. Saif

ABSTRACT

Engineering the behavior of liquids on solid surfaces has wide applications ranging from the design of water-repelling surfaces for daily use to fluid flow manipulation in lab on chip devices and inhibiting corrosion of machinery. Given the ubiquitous interaction of liquids with solids, these applications only represent a drop in the seemingly endless ocean of opportunities. Thus it is not surprising that researchers have been trying to decipher this phenomenon for several centuries now but the complexity of this multi-scale phenomenon has left much to be understood.

Recent advances in micro/nano manufacturing have granted researchers an unprecedented ability to control surface texture and properties. This, combined with the fact that surface forces become increasingly important at small scale, makes it an opportune time to focus studies in the area. Understanding liquid-solid interaction and developing applications around the same has been a central theme of this thesis.

In this work, I have explored the solid-liquid interaction at a fundamental level and developed a thermodynamic model of a liquid drop on a rough surface. The model is validated by several experimental observations from other researchers. Using the model, I have shown that the geometry of roughness features could play an important role in the determination of thermodynamic state of the liquid on the surface as well as characterization of solid surface. Further, I have used this understanding to predict wetting anisotropy on asymmetric sawtooth surface and demonstrated the same experimentally.

I also demonstrate a passive cascadable microfluidic logic scheme. The design is centered around interfacial phenomena and does not require any external power and has no electronic components. The scheme could replace electronic controls in diagnostic systems leading to increased portability and reduced costs. It can also be used in environment harmful for silicon electronics. In another application, geometry based surface patterning is explored in creating wall less flow in microchannels. I have used the latter to add scalability to the passive cascadable logic scheme. Wall less flow could also provide tremendous increase in liquid-gas surface area and open up opportunities to develop liquid-gas reactions systems or possibly ‘self-cleaning’ air-filters.

Dedicated to my wonderful parents

ACKNOWLEDGEMENTS

First and foremost I want to thank my advisor Prof. Nicolas X. Fang. I much appreciate his contribution of time, ideas and funding. He always encouraged me to be independent and challenged me to hone my ideas. His achievements have always inspired me and I am thankful for the excellent example he has provided as a successful professor and researcher.

The members of the Fang group have contributed immensely to my personal and professional time at University of Illinois. I would like to thank: Chunguang Xia, Pratik Chaturvedi, Shu Zhang, Howon Lee, Anil Kumar, Hyunjin Ma, Keng Hsu, Jun Xu and Matthew Alonso for their friendship and good advice. Their hard work has always been a source of inspiration.

I would also like to thank my committee members: Prof. Anthony M. Jacobi, Prof. Paul J. A. Kenis and Prof. Taher A. Saif. They have been very supportive and have always provided me with much valuable guidance.

I am grateful to the staff of MNMS cleanroom: Bruce Flachsbart, Michael Hansen, Glennys Mensing and Adam Sawyer. They have helped me immensely and provided much needed guidance for my work in the cleanroom. I would also like to thank Ankit Raj, Ashutosh Dixit and Huan Li for help with my experiments and device fabrication.

My special thanks to the staff members of Mechanical Engineering at the University of Illinois, especially Kathryn Smith. She has been very cooperative and has gone out of her way to help me.

My time at University of Illinois was made enjoyable in large part due to the many friends who became a part of my life. They have been my family away from home and have provided me with support, encouragement and love. I have immensely enjoyed their company and learnt much from them.

Lastly, I would like to thank my wonderful parents for all their love, encouragement and sacrifice. I am much thankful to my brother and his wife for keeping me cheerful and always being supportive. My extended family has always been very encouraging and supported me in all my pursuits. Special thanks to my loving, encouraging and patient fiancé Neha, whose support during the final stages of this Ph.D. is so appreciated.

TABLE OF CONTENTS

1. BACKGROUND AND MOTIVATION

Engineering the behavior of liquids on solid surfaces has wide applications ranging from the design of 'water-repelling' surfaces to fluid flow manipulation in lab on chip devices and designing better surfaces to inhibit corrosion and prevent fouling. Given the ubiquitous interaction of liquids with solids, these applications only represent a drop in the seemingly endless ocean of opportunities that understanding the behavior of liquids on solids would provide. Thus it is not surprising that researchers have been trying to decipher this phenomenon for several centuries now but the complexity of this multi-scale phenomenon has left much to be understood.

Recent advances in micro/nano manufacturing have granted researchers an unprecedented ability to control surface texture and properties. This, combined with the fact that surface forces become increasingly important at small scale, makes it an opportune time to focus studies in the area. Understanding liquid-solid interaction and developing applications around the same has been a central theme of this thesis.

1.1 Research Objective and Scope

The objective of this research is two fold: (1) To develop a theoretical understanding of wetting on rough/structured surfaces and (2) to use the understanding to develop specific applications - (a) Anisotropic wetting surfaces (b) Cascadable passive microfluidic logic (c) Wall-less flow in microchannels

The first objective stems from gaining a fundamental understanding, from a thermodynamic point of view, of the behavior of liquid on rough/structured surfaces. Liquid-solid interactions are multi-scale, with shaping forces ranging from Van der Walls at the molecular scale to gravity at the macroscopic level. But recent studies have allowed making reasonable approximations and a microscopic modeling of the interaction has been shown to be suffice in explaining certain macroscopic observations. Several researchers have presented such microscopic models in explaining observations like contact angle, which has been shown to represent one of the several metastable states that exists for a liquid drop placed on a rough solid surface. Further, it has been shown that the lowest energy of all such states corresponds to the contact angle determined by Wenzel relation, called the Wenzel angle, and experimental determination of Wenzel angle can be used to characterize solid surfaces. However, researchers have neglected the geometry of surface roughness features in their modeling efforts. In this work the focus has been on developing a thermodynamic model to qualitatively understand the behavior of a drop on rough/textured surfaces by accounting for the effect of geometry of roughness features as the latter could physically limit the states available to the drop and thus modify the associated Gibbs energy barriers.

Further, several applications are developed based upon the results and insights from the study. The first application is related to controlling the direction of wettability of a surface based upon the surface structure. Such surfaces are termed as ‘anisotropic’ and can be useful in manipulating liquid flow with applications in microfluidics.

The second application deals with developing a microfluidics based logic scheme which can be

used to integrate control system into lab-on-chip type devices. Although, microfluidic based logic schemes have been demonstrated in the past but they have either used active devices (like pumps) or haven't been scalable and cascadable. Here, a passive microfluidics based on interfacial phenomena is explored in designing a scalable and cascadable logic scheme. Such a system could lead to cheap use-and-throw diagnostic devices and can also be used in environments which are too harsh for silicon electronics.

In the third application, geometry based surface patterning is explored in creating liquid-walls in microchannels. This could provide tremendous increase in liquid-gas surface area and open up opportunities to develop liquid-gas reactions systems or possibly 'self-cleaning' air-filters.

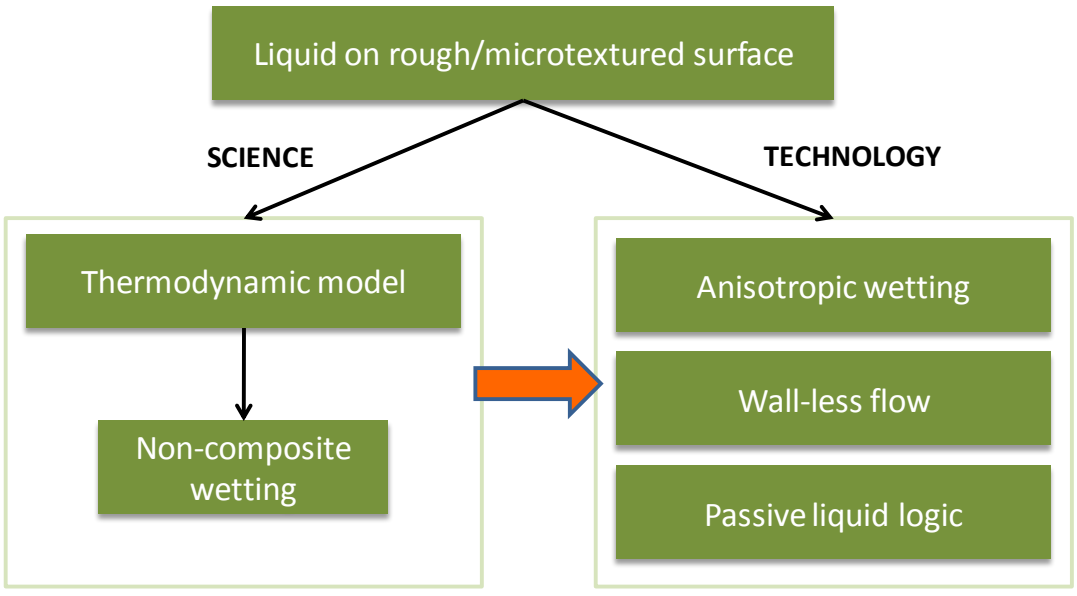

Figure 1.1: Research scope and objective

1.2 Thesis Organization

This thesis is divided into 5 sections. Following this introduction section is section 2, “Thermodynamic modeling of rough surfaces: Role of Gibbs energy barriers”. Section 3 presents, “Design of anisotropic surfaces” based on the thermodynamic model in Section 2. Section 4 details out “Cascadable passive microfluidic logic scheme”. Section 5 entails “Wall-less flow in microchannels”.

2. THERMODYNAMIC MODELING OF ROUGH SURFACES: ROLE OF ROUGHNESS FEATURES

Assessment of the Young's contact angle (YCA) plays an important role in the characterization of solid surfaces by determination of their surface tension. However, common measurement of contact angle usually involves measuring a 'static' contact angle, which is one of the many metastable states available to the drop. It has been suggested that YCA could be determined by experimental determination of the global energy minimum of the drop, which has been shown to correspond to the classical Wenzel angle for 'large' drops. However, the equivalence of global energy minimum and Wenzel angle has only be rigorously proven for a drop infinitely larger than the scale of the roughness, which discounts the geometry of the roughness features and is not realistic.

Here I present the calculations for a drop, much larger than the scale of roughness, and account for the effect of geometry of roughness features. It is shown that the latter could physically limit the states available to the drop. This modifies Gibbs energy barriers and alters global energy minimum so that the latter may not correspond to the Wenzel angle.

2.1 Introduction

Wetting is the process of making contact between a solid and a liquid [1] in a medium which is either vapor or another immiscible fluid. It is ubiquitous in nature and has applications in areas like printing, adhesion, lubrication, painting and many more. Thus, it is not surprising that

researchers have been trying to decipher this phenomenon for more than a century now, but much is left to be understood.

An important and measureable characteristic of wetting systems is the contact angle (CA). It is defined as the angle between the tangent to the liquid–fluid interface and the tangent to the solid interface at the contact line of the three phases [2]. It is usually measured on the liquid side.

On an ideal solid surface, which is smooth, homogeneous, isotropic and non-deformable, the contact angle is correlated to the interfacial tensions by Young's equation [3].

$$\gamma_{SF} = \gamma_{LF} \cos\theta_Y + \gamma_{SL} \qquad <2.1>$$

where, θ_Y, is the Young's contact angle (YCA) and γ_{SF}, γ_{LF} and γ_{SL} denote solid-fluid , liquid-fluid and solid-liquid interfacial energy, respectively. It has been suggested that the molecular interactions between the three phases, in the immediate vicinity of the contact line, alter the interfacial energies between each pair of phases and thus modify Young's equation for ideal surfaces [4, 5]. However, the modification has been found to be significant only for nanoscale drops [6-8] and for larger drops, which would be the focus of this study, equation 2.1 applies as it is.

Assessment of YCA plays an important role in the characterization of solid surfaces by determination of their surface tension [2]. If Gibbs energy of an ideal wetting system (consisting of a liquid drop on an ideal surface) is plotted, it can be shown that YCA represents the unique minimum [1] and thus, is also the equilibrium contact angle. However, most real solid surfaces

are rough and chemically heterogeneous and far from the ideal surface that the YCA was derived for. Therefore, the determination of the actual contact angle (θ_{ac}), which is the angle that the tangent to the liquid–fluid interface subtends with the actual surface of the solid, and its relationship to YCA, is of fundamental interest.

It has been proven theoretically, in a general way that applies to three-dimensional systems, that the actual contact angle of a macroscopic drop at equilibrium, is equal to the YCA [9, 10]. However, with the current experimental methods, it is usually impossible to measure the actual contact angle as the same is either inaccessible on rough surfaces or varies from point to point, at a microscale, due to heterogeneity. Thus, researchers have directed their efforts in finding the relationship between YCA and an experimentally measurable quantity, which is usually the apparent contact angle (APCA), also known as the geometric contact angle (GCA).

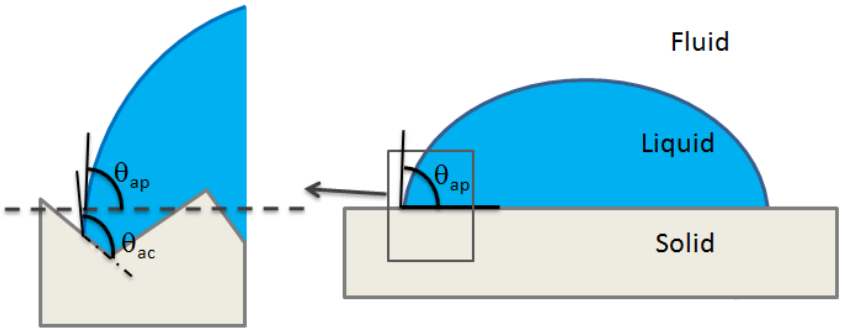

Figure 2.1: Macroscopically observable solid surface is in fact the apparent surface and the macroscopically observable CA is the apparent CA (θ_{ap}).

APCA (θ_{ap}) is defined as the angle that the tangent to the liquid-fluid interface makes with the macroscopically observable solid surface, when the system is at equilibrium (Figure 2.1).

However, it has been found that a range of observable APCAs exist for real surfaces [11-15]. The maximum observable contact angle is called the advancing contact angle, θ_a, and the minimum is termed the receding contact angle, θ_r. The names are apt as these angles are observed when contact line just advances or recedes respectively when liquid is added or removed from a sessile drop. The difference between advancing and receding contact angle is termed as the contact angle hysteresis (CAH). It is not immediately clear as to how to interpret the existence of various APCAs and use the information to determine the YCA and thus it necessary to understand the nature of CAH.

CAH can result due to several factors including surface roughness [13, 14], surface heterogeneity [12, 15], liquid absorption and/or retention [16-18] and presence of liquid film [19]. Since roughness and heterogeneity are common characteristics of real surfaces, they have been investigated most widely. In this paper, the surface is assumed as homogeneous and rough and heterogeneity would be dealt with in future studies. It is also assumed that the liquid fills in the roughness grooves of the surface or in other words, the wetting is homogeneous.

Wenzel [20] was the first to describe the effect of surface roughness on surface wettability by defining a characteristic 'Wenzel angle', θ_W, for rough surfaces as:

$$\cos(\theta_W) = r_{wenzel}*\cos(\theta_Y) \qquad <2.2>$$

where, r_{wenzel} is the ratio of the actual surface area to the geometrically projected surface area. The equation was developed based on an intuitive understanding of wetting by averaging out the details of the rough surface. Shuttleworth and Bailey [13] first pointed out the concept of APCA

and provided a quantitative estimate of CAH. Later, Johnson and Dettre's seminal paper provided a thermodynamic perspective of liquid-fluid-solid interaction on rough surfaces [14]. They modeled a two-dimensional drop placed on an axisymmetric sinusoidal surface and demonstrated the existence of numerous metastable states, which represented different APCAs. They showed that Gibbs energy barriers exist between different metastable states and argued that the droplet will assume a metastable state, and the corresponding APCA, based on the available vibrational energy. Johnson and Dettre also pointed out that when roughness features are small compared to the drop, the global minimum in Gibbs energy can be approximated by the Wenzel angle. Several models with additional considerations like gravity [21] and generalized roughness profiles [22] have been presented since and have corroborated Johnson and Dettre's results.

Recently, Wolanski et al. [23] have shown mathematically that for 'drops infinitely large compared with the scale of the roughness,' Wenzel angle does indeed correspond to the 'global minimum' in Gibbs energy. Although they have not calculated how large the drop should realistically be, a ratio of two to three orders of magnitude seems sufficient [24].

Thus, it has been suggested that if the global energy minimum is determined experimentally, YCA can then be calculated using the Wenzel equation. A few methods have been used by researchers to experimentally determine the global energy minimum, most notably by placing a drop on a rough surface and subjecting it to vibrations. This allows the drop to overcome Gibbs energy barriers and reach the 'system equilibrium' or the 'most stable' state, which will correspond to global energy minimum. However, the parameters used to identify the 'most stable state' have not been completely and conclusively established. Furthermore, the relation between

the ‘global energy minimum’ and Wenzel angle has only been rigorously proven for an infinitely large drop – which is far from a realistic case.

In this study, I present a simplified thermodynamic model of a drop on a rough surface, with the drop much larger than the scale of roughness. The geometry of the roughness features is accounted for in the model and it is shown that it physically restricts access to various states that would have been otherwise available to the drop. The effect of the same on Gibbs energy barriers and Gibbs energy profile of the system is further explored.

2.2. Theory

Consider a drop sitting on a rough surface with isosceles triangular roughness features. The particular roughness features have been assumed for ease of calculations and the model developed henceforth shall apply similarly to other roughness geometries.

The following assumptions are made –

1. Solid surface is non-deformable and chemically homogeneous.
2. Roughness features are infinitely long and extend in direction perpendicular to the paper.
3. Volume of the drop is constant.
4. Drop is long and cylindrical.
5. Drop is ‘large’ so that line tension can be ignored [6-8]
6. It is assumed, on physical grounds, that the vertices of the roughness profile are rounded over a very short distance

7. Drop wets the solid in the grooves i.e. wetting regime is non-composite
8. Drop is in thermal equilibrium with the surroundings and there are no external forces. Chemical reactions are neglected.
9. Dynamic effects due to motion of contact line have been neglected.
10. Adsorbed liquid and liquid-film contribution to contact angle hysteresis are neglected
11. Effect of gravity is negligible
12. Drop is surrounded by air at standard temperature and pressure STP

Using the above assumptions, the drop can be assumed to be two dimensional (2-D). The schematic of the 2-D wetting system is shown in Figure 2.2. Although a 2-D model is simplistic, the attempt is here is to illustrate general features of the wetting system. Similar 2-D models have been previously employed by researchers [14,25-28] and several trends have been validated by experimental observations. For further discussion on experimental validation, please refer to section 4.

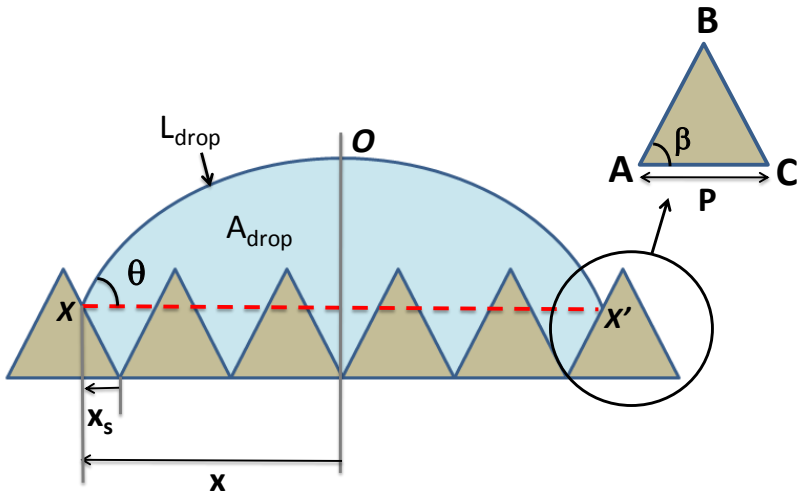

Figure 2.2: Schematic of two-dimensional drop on a rough surface (x – distance of contact line from center, P – roughness pitch, θ – geometric/apparent contact angle for a given x and A_{drop})

To model the system, the equation that relates the Gibbs energy of the system to the geometric contact angle (GCA) of the drop is derived. In Figure 2.2, GCA is the angle θ that the tangent to the drop-air interface at X or X' subtends with the apparent surface, represented by the horizontal line XX', at a given value of x. It is also referred to as the apparent contact angle (APCA) in literature.

The Gibbs energy (GE) of the solid-liquid system can be calculated by considering the contribution of the interfacial energies due to liquid-air (LA), liquid-solid (SL) and the unwetted solid-air (SA) areas [25] –

$$GE = \gamma_{SA} A_{SA} + \gamma_{SL} A_{SL} + \gamma_{LA} A_{LA} \qquad <2.3>$$

For the 2D droplet, the solid-liquid area (A_{SL}) per unit length of the drop is given by the wetted length of surface roughness features, s –

$$s = 2 * \left(\frac{x}{\cos \beta} \right) \qquad <2.4>$$

The liquid-air area (A_{LA}) per unit length of the 2D drop is the perimeter of the drop-air interface, L_{drop} –

$$L_{drop} = 2 * \theta * \left(\frac{x}{\sin \theta} \right) \qquad <2.5>$$

With the given assumptions, Young's equation is locally valid [6-10] and equation 2.3 can be simplified to obtain relative Gibbs energy per unit length of the drop:

$$GE = \gamma_{LA} * (-\cos\theta_Y * s + L_{drop}) + \gamma_{LA} * L_{SA} \quad <2.6>$$

Where, L_{SA} is the total area of solid surface (A_{SA}) per unit length of the surface. Since L_{SA} is constant for the given problem, it is hereby ignored and the Gibbs energy of the system is referred to as the 'relative' Gibbs energy (equation 2.7). Further, to normalize, γ_{LA} has been assumed to be 1. It should be noted that equation 2.7 is similar to the equation derived by Johnson and Dettre [14].

$$GE_{rel} = (-\cos\theta_Y * s + L_{drop}) \quad <2.7>$$

A relation can be obtained between GCA (θ) and x by imposing constant volume constraint. The volume of the drop per unit length, A_{drop} (Figure 2.2) is given as:

A_{drop} = Vol. of OXX' – Vol. of roughness features above XX' + Vol. of liquid below XX'

Using simple geometry it can be shown that:

$$\text{Volume of OXX'} = \left[\theta * \left(\frac{x}{\sin\theta}\right)^2 + \frac{x^2}{\tan\theta}\right] \quad <2.8>$$

$$\text{Volume of Roughness features above XX'} = \left[(N-1) * 2 * \frac{(2x_s)^2 * \tan\beta}{2}\right] \quad <2.9>$$

$$\text{Volume of liquid below XX'} = \left[N * 2 * \frac{(P - 2 * x_s)^2 * \tan\beta}{2} \right] \qquad <2.10>$$

where, N = x/P rounded off to the lowest integer and $x_s = (x/P - N)*P$

Thus, for a given x, θ is calculated, which is then substituted in equation 2.6 to calculate the relative Gibbs energy of the drop. Thereby x is varied and a plot of relative Gibbs energy is obtained for varying θ.

For this study, the roughness pitch has been assumed as 10 μm. Initial GCA and x have been assumed to be 5 Deg. and 5000 μm respectively. This results in a drop volume that corresponds to a circular 2D droplet with diameter ~ 5.5 mm, which is around 550 times the pitch of roughness features. The volume of the roughness features is ~3% the volume of the drop.

I model two cases, one with $\beta = 50^o$ and the other with $\beta = 60^o$. Young's angle is assumed to be 70^o. Calculation for Young's angle > 90^o are not shown, but will follow in a similar fashion.

2.2.1 CASE I: $\beta = 50^o$ and P = 10 μm

With the given roughness parameters, relative Gibbs energy of the drop can be calculated using equation 2.6 and has been plotted in Figure 2.3.

The relative Gibbs energy profile initially appears smooth but a close look (inset) shows that it is sawtooth-like and consists of 'valleys' and 'hills'. The valleys represent local minimum or metastable states and correspond to the state when contact line is at the top vertices of the roughness features, point B in Figure 2.2. The hills represent local maxima or unstable states and correspond to the state when the contact line is at the bottom vertices of roughness features, points A or C in Figure 2.2. It should be noted that since the top and bottom vertices are rounded over a very short distance, they allow the Young's contact angle to be locally valid for a given GCA.

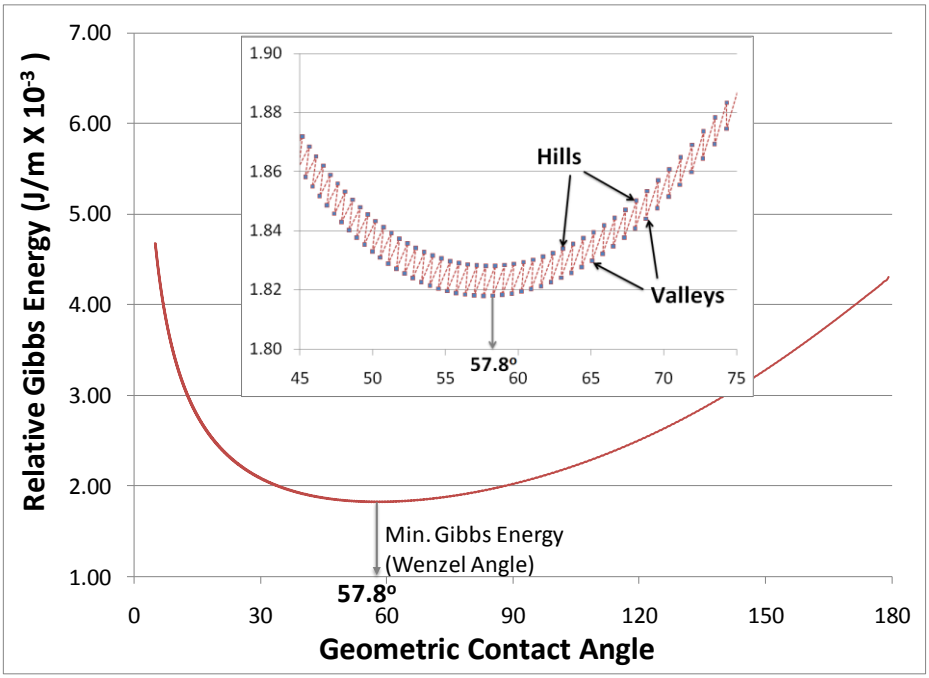

Figure 2.3: Relative Gibbs energy vs. geometric contact angle for triangular roughness profile with P = 10 μm, β = 50°, circular 2D water drop with diameter ~ 5.5 mm, θ_Y = 70°. Inset: Zoomed in image

The difference in the relative Gibbs energy of a valley (metastable state) and the adjacent hill (unstable state) is called Gibbs Energy Barrier (GEB) and represents the energy required by the drop in a given valley to jump to the adjacent valley. If the adjacent valley has a larger GCA, GEB is termed as GEB - larger GCA (GEB-L) and if the adjacent valley has a smaller GCA, GEB is called GEB - smaller GCA (GEB-S). This is shown in Figure 2.4, where GEB-L_1 and GEB-S_1 are the GEBs associated with state 1.

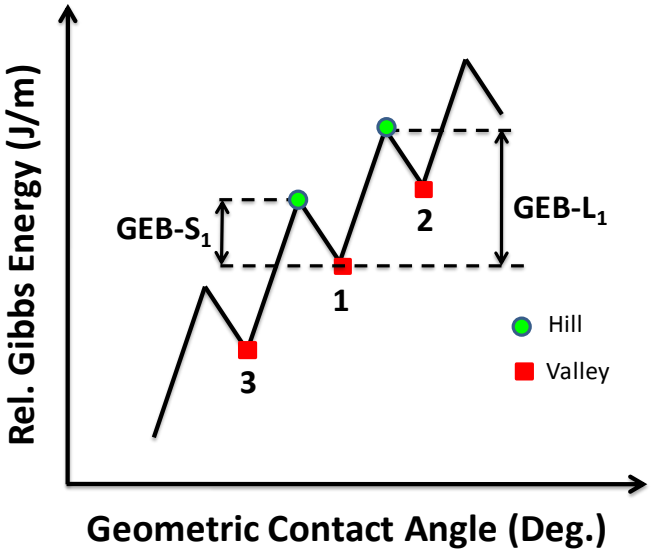

Figure 2.4: Schematic of Gibbs Energy Barrier

The GCAs corresponding to GEB-L = 0 and GEB-S = 0 represent the maximum advancing and minimum receding angles, respectively. Metastable states exist only for GCA values between the maximum advancing and the minimum receding angles. Here, the term maximum and minimum is applied to advancing and receding angle because they represent the limiting metastable states in a system with zero perturbation/external noise.

Figure 2.5 shows the plot of GEB-S and GEB-L. The maximum advancing and the minimum receding contact angle are also shown. It can be seen that the maximum advancing contact angle is (θ_Y + β) and the minimum receding angle is (θ_Y - β), where $\theta_Y = 70^o$ and $\beta = 50^o$. These angles were first determined by Shuttleworth and Bailey [13] and are representative of the fact that the Young's equation is locally valid.

The states represented by the lines joining the valleys and hills correspond to the state of the drop between the vertices A and B or A and C in Figure 2.2. These are 'non-equilibrium' states as the Young's equation cannot be locally satisfied (except for a unique case where GCA = θ_Y). Thus, the relative Gibbs energy associated with these should only be interpreted qualitatively.

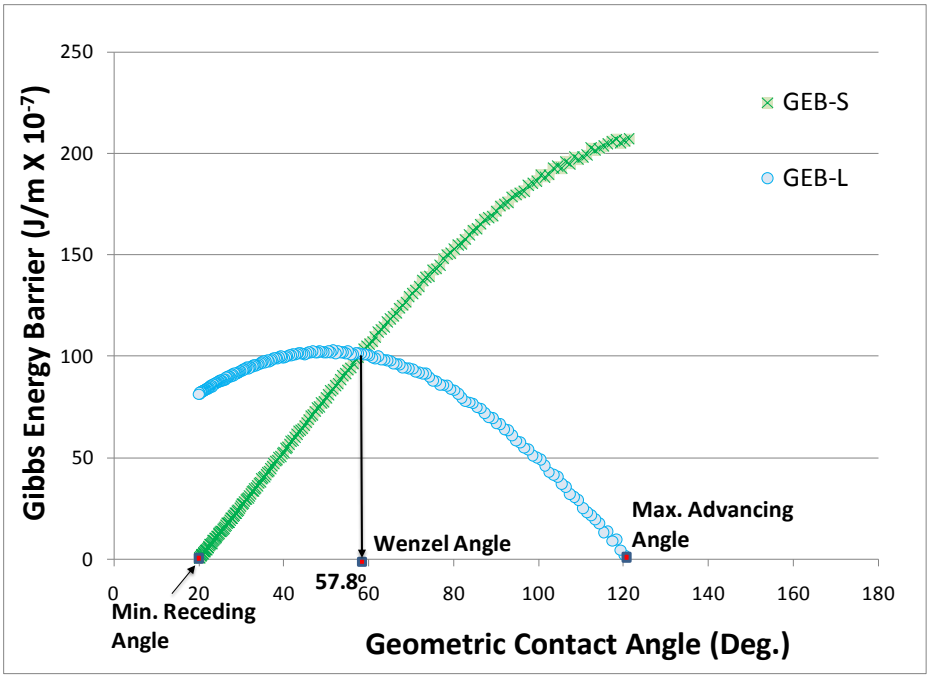

Figure 2.5: Gibbs energy barriers for triangular roughness profile (P = 10 μm, $\beta = 50^o$) and circular 2D water drop with diameter ~ 5.5 mm with $\theta_Y = 70^o$

The GCA with the least Gibbs free energy is shown in Figure 2.3 and 2.5. Although, it is not possible to mathematically determine the angle corresponding to the global minimum Gibbs energy for a metastable system [29], it has been suggested that for 'large' drops, the angle can be approximated by the classical Wenzel angle [14,23,24]. The approximation seems valid for this case as the Wenzel angle is $\theta_W = 57.8^o$. It is interesting to note that the global energy minimum is the state where GEB-S is equal to GEB-L. The reasons for the same would be discussed later.

While plotting Figure 2.3 and 2.5, it has been assumed that all the states are available and accessible to the drop. However, the geometry of roughness features physically restricts access to certain 'unstable' states or hills, which correspond to the state of the drop in the bottom vertices of the roughness features, represented by A and C in Figure 2.2. This modifies Gibbs energy barriers and alters Gibbs energy profile. To demonstrate the same, two situations are considered in this study and described as follows:

Case A: $\theta > (180 - \beta)$

Consider Figure 2.6a where the drop's contact line is at B1 or in other words, the drop is in a metastable state B1. The adjacent hill and valley correspond to the state of drop in vertex C1and B2 respectively and the energy required to 'jump' from B1 to B2 is given by GEB-S for state B1:

$$GEB\text{-}S_{(B1)} = GE_{Rel,C1} - GE_{Rel,B1} \qquad <2.11>$$

The terms on right hand side are calculated using equation 2.6.

But as shown in Figure 2.6b, when $\theta_1 > (180 - \beta)$, the roughness geometry physically restricts the access to the unstable state at C1. The drop can be assumed to intersect B2 as soon as it reaches C2, an intermediate point on the roughness profile. Therefore, the geometry of the roughness features modifies GEB-S of state B1 and the modified value is given as:

$$GEB\text{-}S_{(B1)\,\mathbf{MOD}} = GE_{Rel,C2} - GE_{Rel,B1} \qquad <2.12>$$

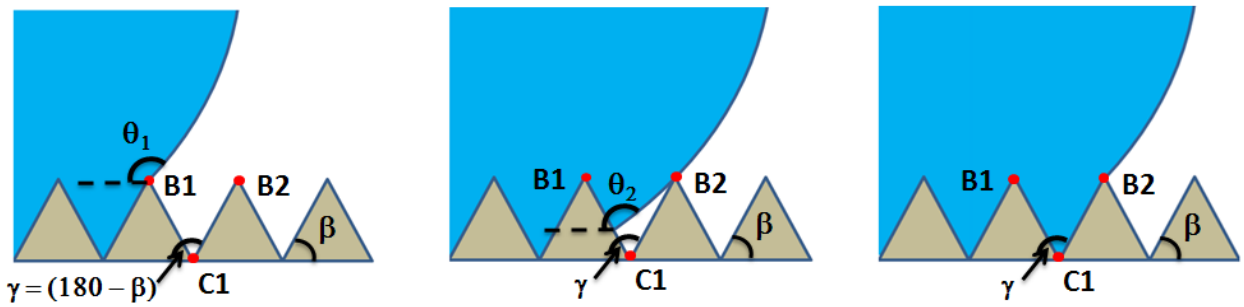

a) b) c)

Figure 2.6: a) Drop with $\theta_1 > (180 - \beta)$ b) Drop 'jumps' to adjacent peak B2 when $\theta_2 > (180 - \beta)$ c) Configuration of the drop after the 'jump'

Since, B1 represents local Gibbs energy minimum and C1 represents local Gibbs energy maxima, therefore the relative Gibbs energy of the intermediate point C2 will lie between the relative Gibbs energy of C1 and B1 or $GE_{Rel,C1} > GE_{Rel,C2} > GE_{Rel,B1}$. Thus, from equations 2.11 and 2.12:

$$GEB\text{-}S_{(B1)} > GEB\text{-}S_{(B1\text{-}B2)\,\mathbf{MOD}} \quad <2.13>$$

Hence, for the given roughness profile, when $\theta > 130^{o}$, the actual GEB-S for state B1 is lower as compared to the value calculated without accounting for the geometry of the roughness features.

Due to the above reasons, GEB-L of state B2 would also be affected and it is assumed that:

$$GEB\text{-}L_{(B2)\,\mathbf{MOD}} = GE_{Rel,B2} - GE_{Rel,C2}. \quad <2.14>$$

Again, it can be shown that:

$$GEB\text{-}L_{(B2)} > GEB\text{-}L_{(B2)\,\mathbf{MOD}} \quad <2.15>$$

It should be noted that since the drop is not at equilibrium at C2, the reduction in GEB-L and GEB-S should be interpreted only qualitatively. For the same reason, Figure 2.6b is just a representative of one of the several possible configurations of the liquid-air interface. The details of the calculation can be found in supplementary material.

Case B: $\theta < \beta$

Another geometric constraint occurs when the GCA is less than β, so that the corresponding unstable state is inaccessible to the drop.

Consider Figure 2.7, when $\theta_1 < \beta$, the unstable state corresponding to the vertex C1 is inaccessible to the drop and it is assumed that, from an initial metastable state B1, the drop can jump to B2 as it reaches an intermediate point C2. In this case, GEB-L for state B1 is affected and it can be shown that the modified Gibbs energy barrier ($\text{GEB-L}_{(B1)\,\mathbf{MOD}}$) is lower than Gibbs energy barrier calculated without taking the geometric constraint into account. Thus,

$$\text{GEB-L}_{(B1)} > \text{GEB-L}_{(B1)\,\mathbf{MOD}}. \qquad <2.16>$$

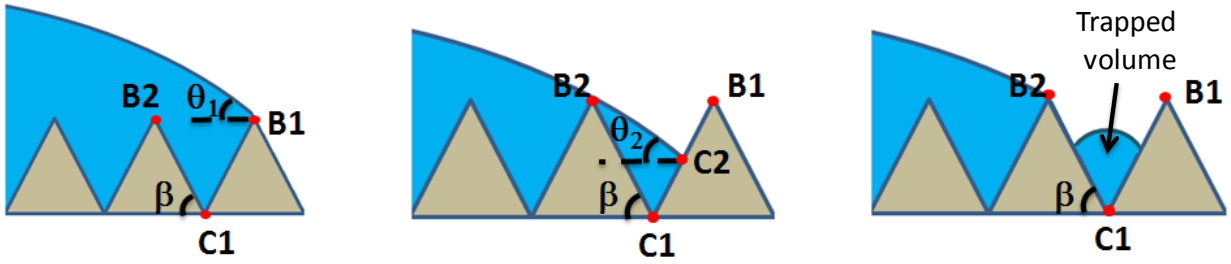

a) b) c)

Figure 2.7: a) Drop with $\theta_1 < \beta$ b) Drop 'jumps' to adjacent peak B2 when $\theta_2 < \beta$ c) Configuration of the drop after the 'jump' with trapped liquid volume

Further, as the drop moves from C2 to the metastable state B2, a small volume of liquid is trapped in the roughness feature (Figure 2.7c). This liquid volume achieves its own equilibrium and subtends the Young's contact angle with the slanted walls of the shown triangular roughness feature. The energy and volume of this trapped liquid is taken into account while calculating Gibbs free energy of the system. Figure 2.8 shows the trapped volume and the change in total volume of the drop for the case being considered. The details of the calculations for the trapped volume can be found in the supplementary material.

GEB-S for state B2 is similarly affected and can be calculated as:

$$\text{GEB-S}_{(B2)\,\mathbf{MOD}} = GE_{B2} - GE_{C2}. \qquad <2.17>$$

As demonstrated earlier, $\text{GEB-S}_{(B2)\,\mathbf{MOD}} < \text{GEB-S}_{(B2)}$; where $\text{GEB-S}_{(B2)} = GE_{B2} - GE_{C1}$

Again, the state of drop at C2 is 'non-equilibrium' and Figure 2.7b is just a representative of one of the several possible configurations of the liquid-air interface. Thus the reduction in GEB-S and GEB-L should be interpreted only qualitatively.

A 'geometric limit' is thus defined as the range of GCAs outside which the Gibbs energy barriers are modified.

The lower and the upper bound of the geometric limit for the roughness features are given by β and $(180 - \beta)$ respectively. For the given roughness profile, the geometric limit exists for $50^o < GCA < 130^o$.

Figure 2.9a shows a plot of relative Gibbs energy for the given roughness profile, both with and without accounting for the 'geometric limit'. It can be seen that for this case, the global energy minimum of the wetting system is unaffected and is given by the Wenzel angle.

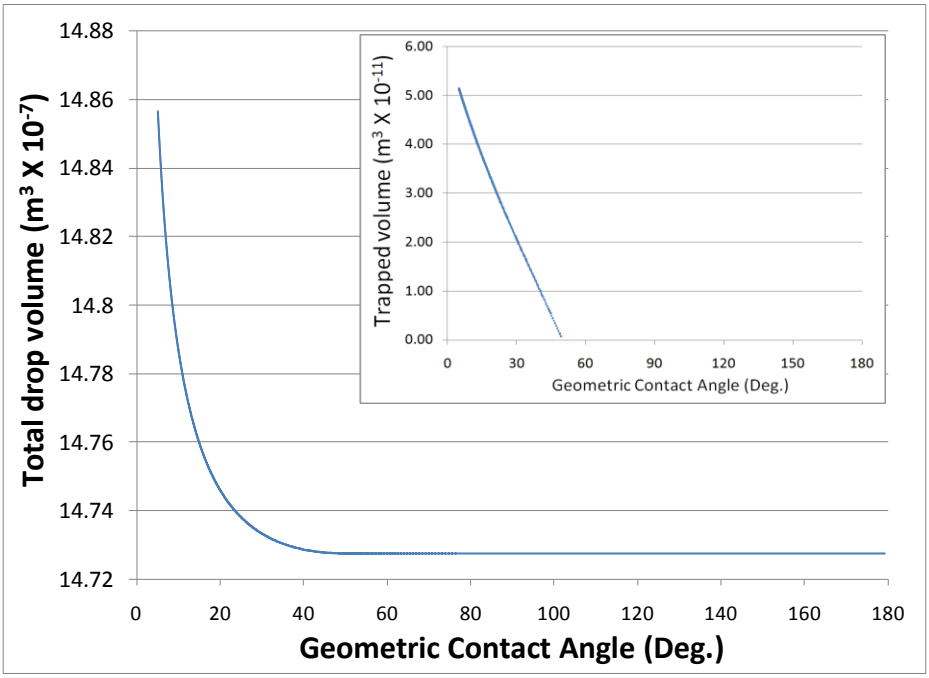

Figure 2.8: Total volume and trapped volume (inset) as a function of GCA for triangular roughness profile (P = 10 μm, $\beta = 50^o$) and circular 2D water drop with diameter ~ 5.5 mm with $\theta_Y = 70^o$.

Figure 2.9b shows the GEBs. Circles and crosses represent GEB-S and GEB-L calculated without accounting for the geometric limit. Outside the geometric limit, GEB-S and GEB-L are modified, as represented by diamond and square respectively. The modified GEBs should be interpreted only qualitatively. As can be seen, the maximum advancing and the minimum receding angles are unaffected by the modification of GEBs. It should be noted that GEB-L is equal to GEB- S at the GCA corresponding to the global energy minimum, given by Wenzel angle.

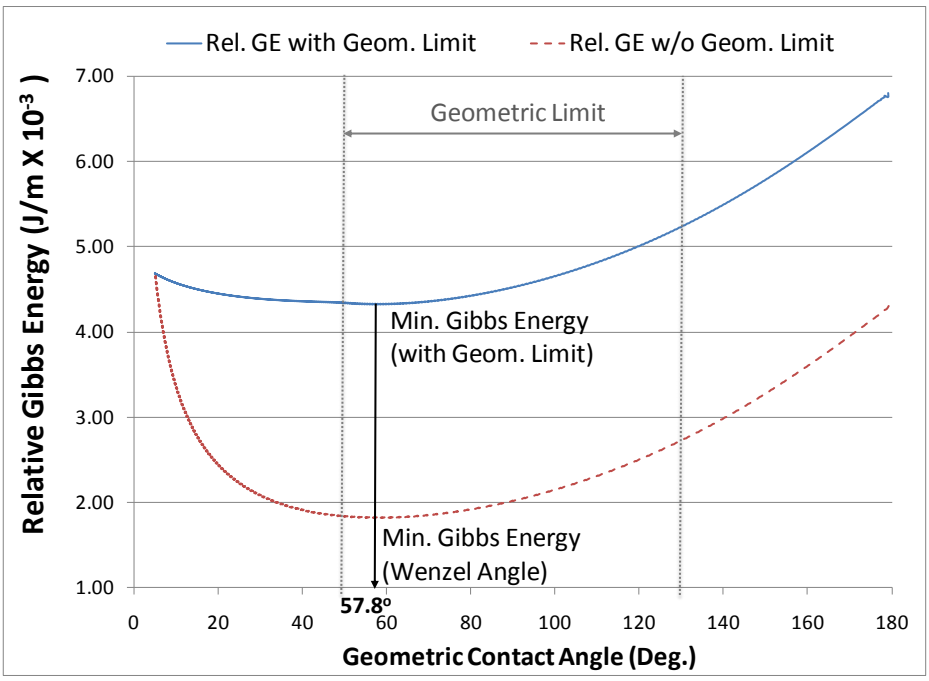

(a)

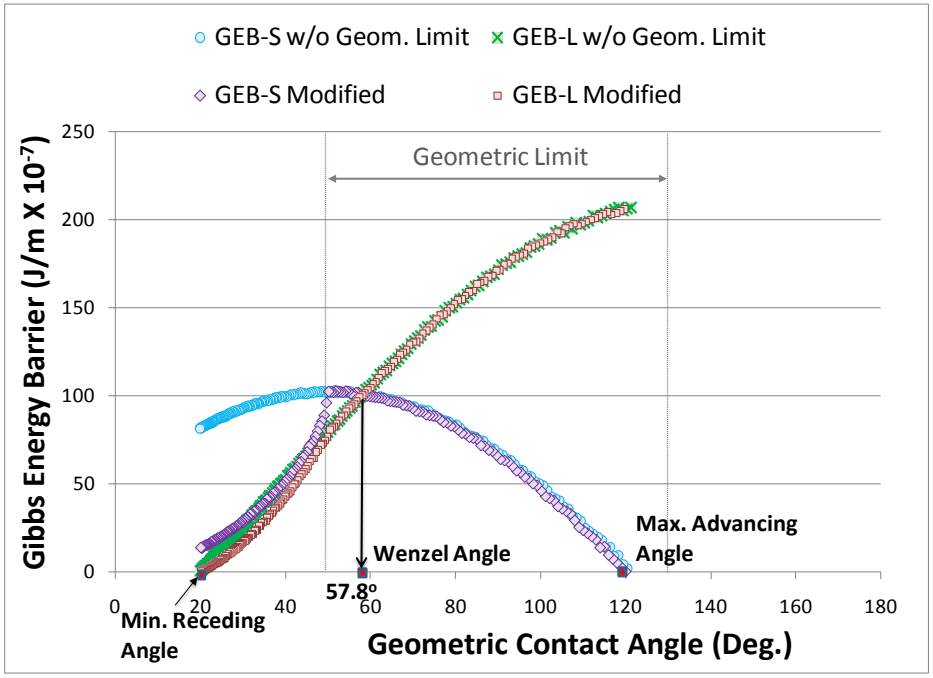

(b)

Figure 2.9: (a) Modified Relative Gibbs Energy and (b) Gibbs energy barriers for triangular roughness profile (P = 10 μm, β = 50^o) and circular 2D water drop with diameter ~ 5.5 mm with θ_Y = 70^o. GEBs remain unchanged inside the 'geometric limit'

Next, calculations are presented for roughness profile with $\beta = 60^o$ and P = 10μm

2.2.2 CASE II: $\beta = 60^o$ and P = 10μm

Similar to the analysis for Case I, roughness configuration with $\beta = 60^o$ is modeled. Figure 2.10 shows the total volume of the drop and trapped volume as a function of GCA.

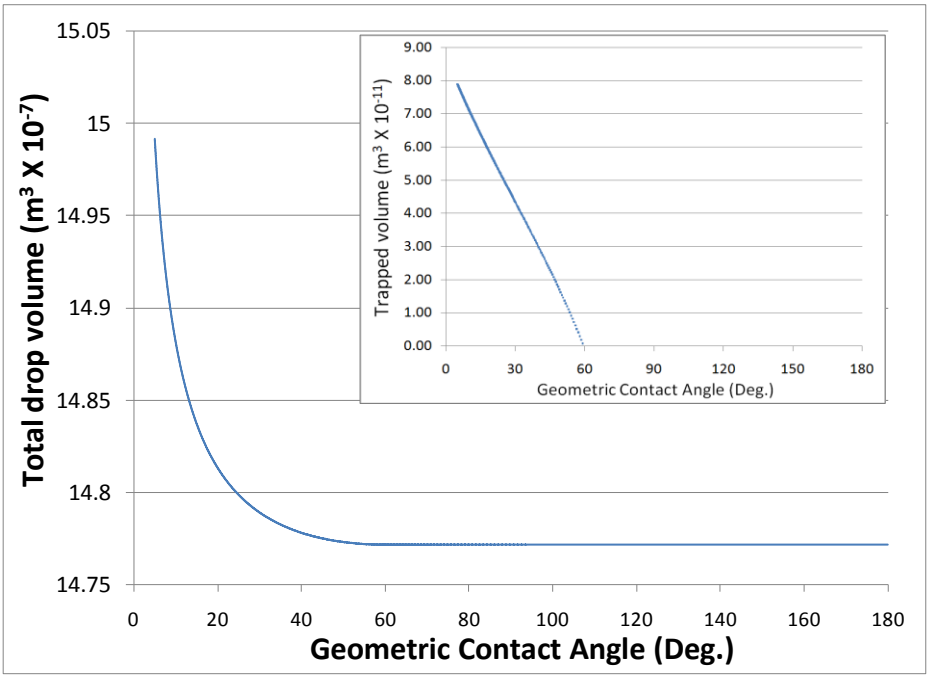

Figure 2.10: Total volume and trapped volume (inset) as a function of GCA for triangular roughness profile (P = 10 μm, $\beta = 60^o$) and circular 2D water drop with diameter ~ 5.5 mm with $\theta_Y = 70^o$.

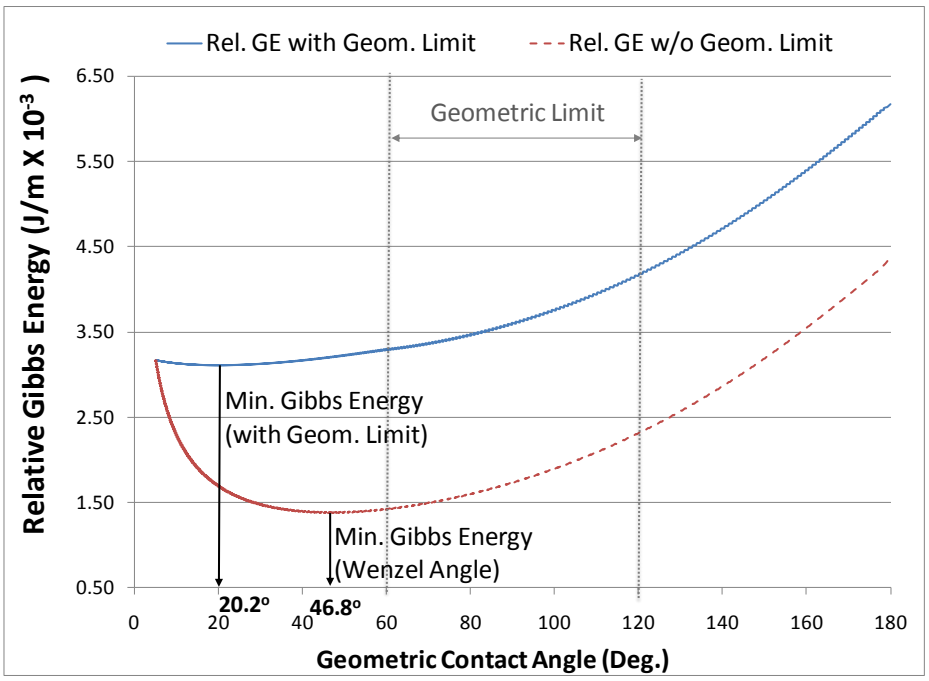

(a)

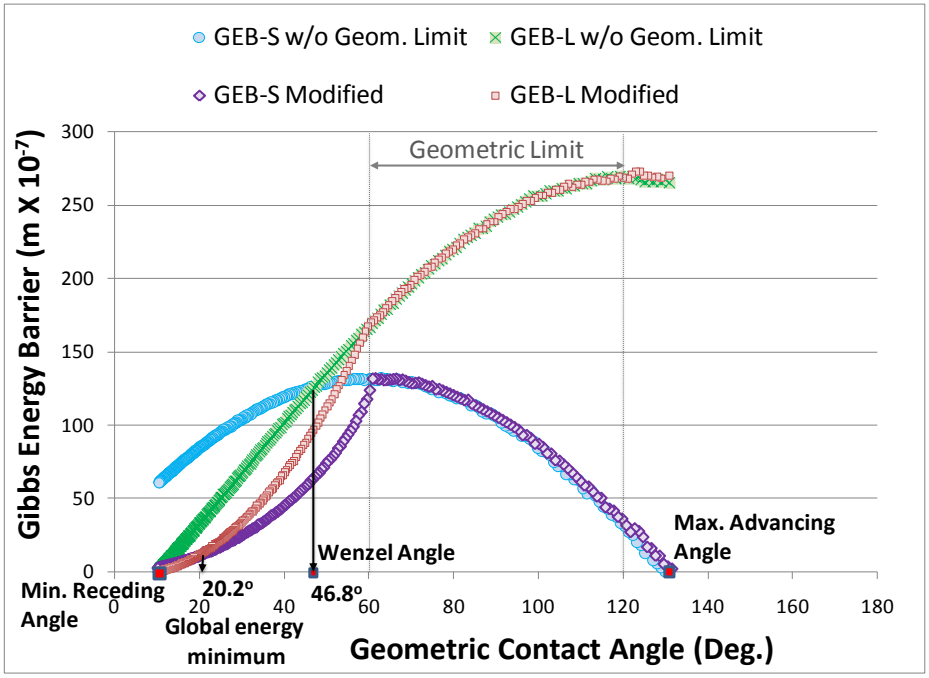

(b)

Figure 2.11: (a) Modified Relative Gibbs Energy and (b) Gibbs energy barriers for triangular roughness profile (P = 10 μm, β = 60°) and circular 2D water drop with diameter ~ 5.5 mm with $\theta_Y = 70^o$. GEBs remain unchanged inside the 'geometric limit'

The upper and lower bounds for the 'geometric limit' are 120^o and 60^o respectively and the relative Gibbs energy and GEBs are shown in Figure 2.10. It can be seen that unlike the previous case, Wenzel angle is not the GCA corresponding to the global energy minimum of the wetting system. This would be discussed in detail in the next section. The GCAs corresponding to zero GEBs represent the minimum receding and the maximum advancing contact angle and are 10^o and 120^o respectively. As earlier, the maximum advancing contact angle is $(\theta_Y + \beta)$ and the minimum receding angle is $(\theta_Y - \beta)$, where $\theta_Y = 70^o$ and $\beta = 60^o$.

2.3 'System equilibrium' state of the drop

'System equilibrium' state is defined as the state which the system will tend to achieve or, if moved away, will tend to return to under perturbations which have a Maxwell-Boltzmann distribution, representative of thermal energy of the molecules at a given temperature. By second law of thermodynamics, the 'system equilibrium' state will always correspond to the global energy minimum. However, for a metastable system, there is no analytical way of determining the global energy minimum [29]. This section explains as to how the 'system equilibrium' state can be determined using Gibbs energy barrier plot and it is shown that modification in the latter could shift the 'system equilibrium'.

For a wetting system, existence of several metastable states was established by early models and experiments [14,15, 30-34] and can be seen from the two cases modeled here. At a given moment, the state in which the drop exists depends on several factors like the method of drop deposition and the history of the drop. Say, the system in a given state is perturbed and at a given

time the magnitude of perturbation is ΔE. Further, assume that the perturbations have a Maxwell-Boltzmann distribution.

Figure 2.12 shows a section of the relative Gibbs energy profile. Assume that state 3 is the current state of the system and the corresponding Gibbs energy of the system = GE_3. The energy required to move the system from state 3 is the difference in Gibbs energy of state 3 and an adjacent 'hill' – which is either 4 or 2. This difference is given by the GEBs as shown. For simplicity, it is assumed that $GEB\text{-}L_5 = GEB\text{-}L_3$

Under perturbation ΔE, there could be three scenarios:

Case 1: $\mathbf{\Delta E} < GEB\text{-}S_3$

Case 2: $GEB\text{-}L_3 > \mathbf{\Delta E} > GEB\text{-}S_3$

Case 3: $\mathbf{\Delta E} > GEB\text{-}L_3$

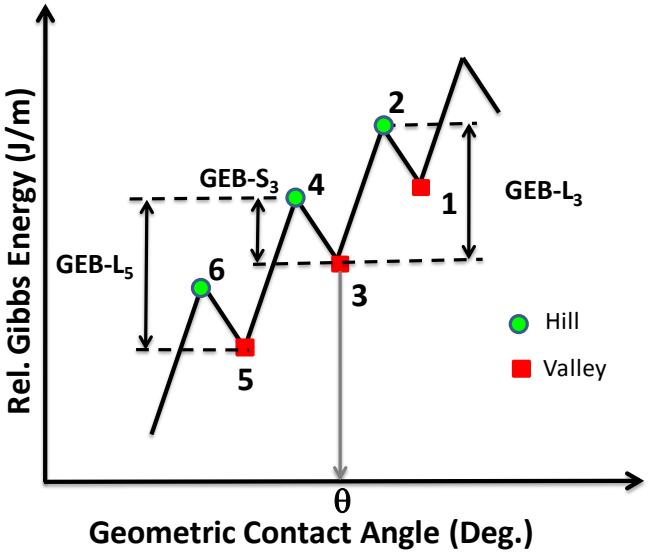

Figure 2.12: Section of Gibbs Energy profile

In Case 1, the system maintains status quo as it does not have enough energy to reach either state 4 or 2. In Case 2, the system attains state 4 and either comes back to state 3 or goes to state 5. If the system goes to state 5, it does not have enough energy to come back to state 3 as GEB-L_5 > ΔE and therefore, either the system stays in state 5 or it could move to a state with a smaller GCA depending on the energy barrier required to do so. In Case 3, the system could either move to state 4 or state 2 and either return to state 3 or move to state 5 or state 1. If the system moves to state 5 or state 1, it again has enough energy to return to state 3.

As the perturbations are Gaussian, a perturbation with lower magnitude is more likely a higher magnitude one. Therefore, since the perturbation required to move to state 5 is smaller than the one required to move to state 1, it is more likely for the system to move to state 5 as compared to state 1. For a general case, if Gibbs energy barrier (GEB) required to move to a state with lower geometric contact angle is less than the GEB required to move to a state with higher geometric contact angle, over time, the system moves to a state with lower geometric contact angle. A similar argument will hold if the inverse is true. Thus, to understand the dynamics of the system, the variation of GEBs for the two cases, modeled here, needs to be understood.

2.3.1 CASE I ($\beta = 50^o$ and P = 10μm)

For this case, the following observations can be made from Figure 2.9b:

1. Wenzel Angle lies *inside* the ‘geometric limit’
2. GEB-S = GEB-L at the Wenzel angle

To start with, assume that the drop is in a metastable state corresponding to a GCA lower than Wenzel angle. This state is to the left of the Wenzel angle in Gibbs energy barrier plot (Figure 2.9b) and it can seen that for such a state GEB-L is lower than GEB-S. As explained earlier, over time, the system would move to a higher GCA and such a movement will continue until the drop reaches the state where GEB-L is equal to GEB-S, which in this case corresponds to the Wenzel state. A similar argument would apply when the initial state corresponds to a GCA greater than the Wenzel angle. Again, the drop would try to attain the Wenzel state where GEB-S is equal to GEB-L. Further, if the system is moved away from the Wenzel state, in either direction, it will tend to return back. Thus, for this case, Wenzel state is the 'system equilibrium' state. Thus, in this case the modification of GEBs does not play a role in determination of the 'system equilibrium' angle.

It can be seen from Figure 2.9a that Wenzel state is also the state corresponding to the global energy minimum of the system. This is no coincidence but follows from second law of thermodynamics. It can be shown a perpetual motion machine can be created if the 'system equilibrium' state does not correspond to the global energy minimum.

2.3.2 CASE II ($\beta = 60^o$ and P = 10μm)

For this case, the following observations can be made from the Figure 2.11 –

1. Wenzel Angle lies *outside* the 'geometric limit'
2. Due to the modification of GEBs, GEB-S and GEB-L are equal at a GCA different from the Wenzel Angle.

Using similar arguments as earlier, it can be shown that over time, the drop tends to move towards the state where GEB-L and GEB-S are equal. Due to modification of GEBs, this state is different from the Wenzel state (Figure 2.11b). Thus, in this case, the 'system equilibrium' angle does not correspond to the Wenzel angle.

Also, it can be seen from Figure 2.11a that Wenzel state is not the state corresponding to the global energy minimum of the system. This state is represents GCA for which GEB-S is equal to GEB-L and again this follows from second law of thermodynamics. Thus, a generalized set of condition for isosceles triangular roughness features can be stated as:

If, $\beta < \theta_W < 180 - \beta$; then θ_W = 'System equilibrium' angle

$\theta_W < \beta < 180 - \beta$; then $\theta_W \neq$ 'System equilibrium' angle

$\beta < 180 - \beta < \theta_W$; then $\theta_W \neq$ 'System equilibrium' angle

Where, slope of triangular roughness feature = β, Wenzel angle = θ_W.

When $\theta_Y < 90^o$, the above relations reduce to: if $\beta < \theta_W$; only then θ_W = 'System equilibrium' angle. This is plotted in Figure 2.13. Although Young's angle can't be directly measured, it represents the hydrophilicity of the surface and is inversely related to the latter. The regime marked as 'complete wetting' represents the area where numerically Wenzel angle ≤ 0, since $\theta_Y \leq \cos^{-1}(1/r)$.

It can be seen that for isosceles triangular roughness features, when geometric limit is taken into account, the range of applicability of Wenzel relation doesn't change appreciably unless when

roughness features are sharp. However, real surfaces consist of both sharp and blunt three dimensional roughness features. Such surfaces can't be modeled by simply averaging out the roughness features into a roughness factor, r as geometry could significantly modify the Gibbs energy barriers and play an important role in determination of 'system equilibrium'. For such surfaces, it is not immediately apparent as to if the Wenzel angle would correspond to the 'system equilibrium' angle (global energy minimum state) and experimental validation is necessary.

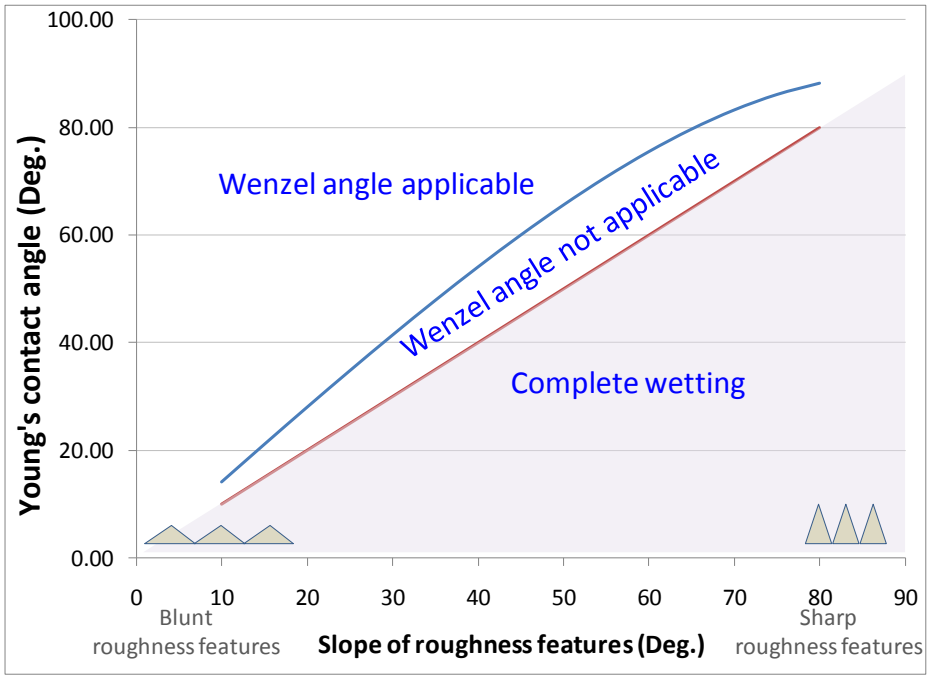

Figure 2.13: Applicability of Wenzel relation for hydrophilic surface with isosceles triangular roughness features

2.4 Comparison with experimental data

Several studies [24, 30-34] have attempted the experimental determination of 'system equilibrium' contact angle for rough surfaces, yet the same remains an open problem. However, experiments have helped elucidate some key aspects of the nature of liquid-solid interaction which allow comparison of the modeling effort and the experimental studies for rough surfaces. These are presented below -

1. Multiple metastable states: The existence of multiple metastable states of a sessile drop on a rough surface is very well known [30-33] and supported by the current model.

2. Effect of vibrations on contact angle hysteresis: Experimental studies [31-33] have reported the reduction of contact angle hysteresis in presence of vibrations. This matches well with the predictions from the model that vibrational energy allows the drop to overcome Gibbs energy barriers, thus reducing the advancing angle and increasing the receding angle and thereby reducing the contact angle hysteresis.

3. Distribution of Gibbs energy barriers: Volpe et al. [32] added vibrations to a standard Wilhelmy microbalance experiment to obtain a 'system equilibrium' state of the meniscus on rough and/or heterogeneous surfaces. They showed that Gibbs energy barriers increase going toward the absolute Gibbs energy minimum. This result matches with the predictions from the model for Case I ($P = 10\mu m$ and $\beta = 50^o$). However, there is still debate over the method used to experimentally determine the 'system equilibrium' state. Further, the model presented here shows that it is not necessary that the Gibbs energy barriers would always increase going to

the ‘system equilibrium’ state (Case II: P = 10μm and β = 60^o) and careful experiments are required to validate the same.

4. Advancing and Receding angles: The values of advancing and receding contact angles match the predictions by Shuttleworth and Bailey, which have been experimentally shown to be relevant [34,35].

5. Reproducibility of advancing and receding angles: It has been observed during experiments [36] on hydrophilic substrates, that receding angle measurements are difficult to reproduce as compared to advancing angles. This could be attributed to the model’s prediction that there are numerous metastable states for contact angles close to receding value while higher contact angles, close to the advancing value, have fewer metastable states. This can be seen in Figure 2.14.

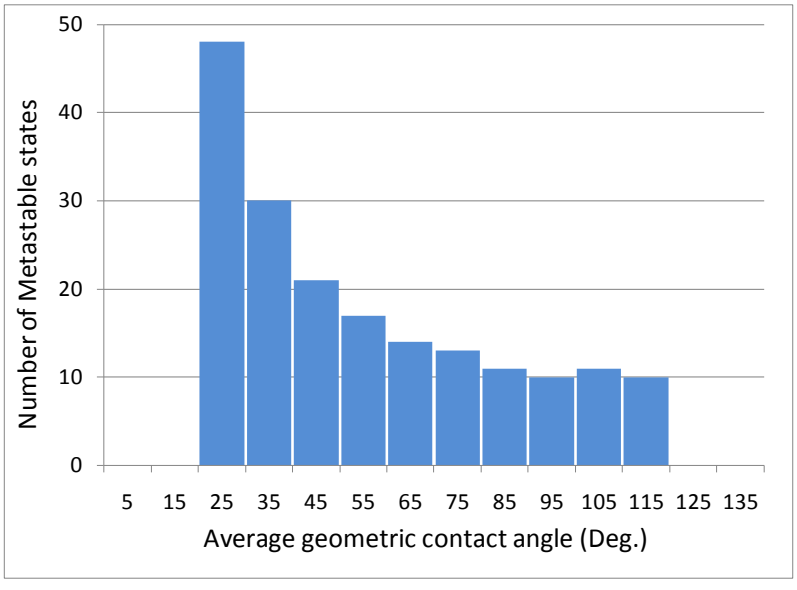

Figure 2.14: Histogram of metastable states for the same surface as used in Figure 2.11. Each bar represents the number of metastable states for a GCA range of +/- 5 degrees.

6. Relation between Wenzel angle and global energy minimum (GEM): Researchers have suggested measuring the ‘system equilibrium’ state of the drop, which will correspond to the GEM, by placing a drop on a rough surface and subjecting it to vibrations. As the drop overcomes Gibbs energy barriers, it tries to reach the ‘system equilibrium’ state. However, no conclusive guideline has been established to recognize the ‘most stable state’.

   Wolanski et al. [37] proved mathematically that when the drop is sufficiently large compared to the roughness scale, it becomes axisymmetric as it reaches the GEM. Meiron et al. [24] used the opposite but unproven statement that is: “following vibrations when a large drop on a rough surface becomes round, it is at the global minimum in energy”, as the working hypothesis to identify GEM. They measured apparent contact angle on homogeneous surfaces of varying roughness by vibrating a sessile drop. They used data only from axisymmetric drops to calculate the contact angle from drop’s diameter and weight. Their measurements of ‘most stable’ contact angle matched well with the global energy minimum calculations, as approximated by Wenzel angle, for the rough surfaces. However, the empirical evidence is not conclusive as the parameters used to identify the ‘most stable state’ have not been completely and conclusively established.

   Further, it is shown in this study that since several states are inaccessible to the drop, Gibbs energy barriers are modified and global energy minimum may not correspond to the Wenzel angle. However, as pointed out, this shift in ‘system equilibrium’ state from the Wenzel state

may only occur for surfaces with sharp roughness features and careful experiments are required to test this conclusion.

2.5 Conclusions

The study presents a two dimensional thermodynamic model for a drop, in a non-composite state, on a rough hydrophilic surface (Young's angle < 90^o) with triangular features. Due to the simplistic nature of model, similar to other two-dimensional models [14,25-28], the attempt is to illustrate general features of a wetting system.

The model reaffirms the existence of several local equilibrium states for a drop placed on a rough surface. However, it is pointed out that, due to the geometry of roughness features, the drop is physically unable to access all the local equilibrium states. This leads to reduction in the Gibbs energy barriers for the metastable states outside the defined 'geometric limit'. It is further shown that if the Wenzel angle lies outside the 'geometric limit,' it will not correspond to the global energy minimum.

For real surfaces, the result could mean that the Wenzel equation might hold only for surfaces with weak roughness, where small and blunt roughness features result in a large 'geometric limit', or surfaces with weak hydrophilicity, where Wenzel angle is large. For hydrophobic surfaces, it can be shown that the Wenzel angle might hold only for either weakly hydrophobic surfaces or surfaces with weak roughness.

Although a quantitative estimate of the reduction in Gibbs energy barriers cannot be obtained, calculations here demonstrate a trend. In cases where Wenzel angle doesn't correspond to the 'system equilibrium' state, a theoretical determination of global energy minimum is not possible and the same would have to be measured experimentally. However, such a measurement might be useless in the estimation of Young's contact angle as there may not be any single analytical equation which could relate the two for surfaces of different roughness.

Supporting Information Available

Appendix A shows the calculation of trapped volume and the modification in Gibbs energy barriers due to the geometry of roughness features.

2.6 References

1. A. Marmur, Annu. Rev. Mater. Res. 39 (2009) 473.
2. A. Marmur, SoftMatter 2 (2006) 12
3. T. Young, G. Peacock, editor. Miscellaneous works, London' J. Murray, Vol. 1, 1855
4. J.W. Gibbs 1961. The Scientific Papers of J. Willard Gibbs, Vol. 1. New York: Dover Publ.
5. A. Marmur, Contact angle and thin film equilibrium. J. Colloid Interface Sci. 148 (1992) 541.
6. A.Marmur, B. Krasovitski, Langmuir 18 (2002) 8919.
7. T. Pompe, A. Fery, S. Herminghaus, J. Adhes. Sci. Technol. 13 (1999) 1155.
8. A.Marmur, J. Colloid Interface Sci. 186 (1997) 462
9. G. Wolansky, A. Marmur, Langmuir 14 (1998) 5292
10. P.S. Swain, R. Lipowsky, Langmuir 14 (1998) 6772

11. D. Li., A.W. Neumann. In: A.W. Neumann, J.K. Spelt, editors. Applied surface thermodynamic. New York' Marcel Dekker, Inc.; 1996. Chapter 3.
12. A.W. Neumann, R.J. Good, J. Colloid Interface Sci. 38 (1972) 341.
13. A. R. Shuttleworth, G. L. Bailey, J. Discuss Faraday Soc 3 (1948) 16.
14. R. E. Johnson Jr, R. H. Dettre, Adv. Chem. Ser. 43 (1964) 112.
15. R. E. Johnson Jr, R. H. Dettre, J. Phy Chem. 68 (1964) 1744.
16. C.N.C. Lam, R.H.Y. Ko, L.M.Y. Yu, A. Ng, D. Li, M.L. Hair, A.W. Neumann, J. Colloid Interface Sci. 243 (2001) 208.
17. C.N.C. Lam, N. Kim, D. Hui, D.Y. Kwok, M.L. Hair, A.W. Neumann, Colloids Surf. A Physicochem Eng Asp. 189 (2001) 265.
18. C.N.C. Lam, R. Wu, D. Li, M.L. Hair, A.W. Neumann, Adv. Colloid Interface Sci.96 (2002) 169.
19. E. Chibowski, Adv. Colloid Interface Sci.103 (2003)149.
20. R.N. Wenzel, Ind. Eng. Chem. 28 (1936) 988.
21. J. D. Eick, R. J. Good, A. W. Neumann, J. Colloid Interface Sci., 53 (1975) 235.
22. C. Huh, S. G. Mason, J. Colloid Interface Sci. 60 (1977) 11.
23. G. Wolansky, A. Marmur, Colloids Surf. A 156 (1999) 381.
24. T. S. Meiron, A. Marmur, I. S. Saguy, J. Colloid Interface Sci. 274 (2004) 637.
25. A. Marmur, Langmuir, 19 (2003) 8343.
26. A. Marmur, E. Bittoun, Langmuir 25 (2009) 1277.
27. J. Long, M.N. Hyder, R.Y.M. Huang, P. Chen, P., Adv. Colloid Interface Sci., 118 (2005) 173.
28. W. Li, A. Amirfazli, J. Colloid Interface Sci, 292 (2005) 195.

29. A. Marmur, Adv. Colloid Interface Sci., 50 (1994) 121.

30. B. T. Lloyd, G. M. Connelly, J. Adhesion, 63 (1997) 141

31. C. D. Volpe, D. Maniglio, M. Morra, S. Siboni, Oil Gas Sci. Technolgy 56 (2001) 9

32. C. D. Volpe, D. Maniglio, M. Morra, S. Siboni, Colloids Surf. A: Physicochem. Eng. Asp. 206 (2002) 47.

33. X. Noblin, A. Buguin, F. Brochard-Wyart, Eur. Phys. J. Special Topics 166 (2009)

34. J.F. Oliver, C. Huh, S.G. Mason, J. Colloid Interface Sci. 59 (1977) 568

35. S. Veeramasuneni, J. Drelich, M.R. Yalamanchili, G. Yamauchi, Polym. Eng. Sci. 36 (1996) 1849

36. H. Y. Erbil, G. McHale, S. M. Rowan, M. I. Newton, Langmuir 15 (1999) 7378

37. G. Wolansky, A. Marmur, Colloids Surf., A 156 (1999) 381.

3. ANISOTROPIC WETTING SURFACES

3.1 Introduction

Anisotropic wetting surfaces have special wetting characteristics as they favor wetting in certain directions more than the others. These surfaces have several possible application e.g. in microfluidics, preferential drainage in air-conditioning evaporators, evaporation-driven deposition etc.. Wetting anisotropy has been demonstrated both chemically [1] and using predefined surface structures [2-6] and the scope of this study is limited the design of anisotropic surfaces based on the latter.

Several studies have been carried out to design and model anisotropic surfaces based on surface structure but most of them have been concerned with micro/nano scale parallel grooved structures [2-6] which provide orthogonal anisotropy - that is the advancing and/or receding angles are different in directions perpendicular and parallel to the grooves as shown in Figure 3.1.

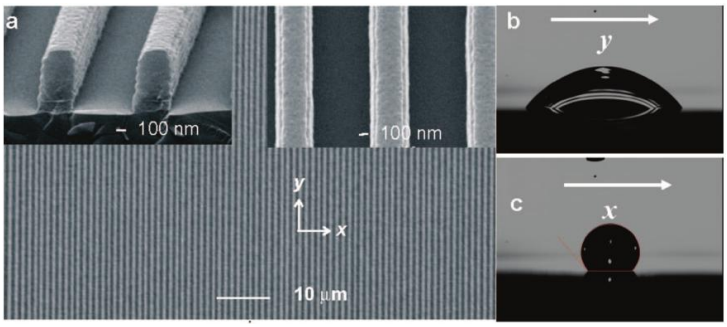

Figure 3.1: Parallel grooved structures showing orthogonal anisotropy. Insets b) and c) show the difference in the shape of the drop when it is placed parallel and perpendicular to the grooves respectively [2]

There have been very few studies in left-right anisotropy and those have been mostly limited to hair/fiber like structures [7]. For a grooved structure, left-right anisotropy implies that the advancing and/or receding angles depend on the direction of measurement perpendicular to the grooves. This is shown in Figure 2.2.

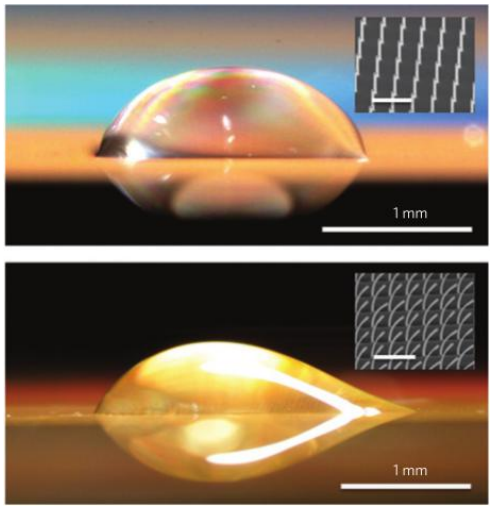

Figure 3.2: Left-right anisotropy in bent hair like structures [7]

Based upon the results from the model developed in the earlier section, left-right anisotropic structures are proposed and characterized in this work.

3.2 Theory

In earlier study, a thermodynamic model was developed for a drop placed on a rough surface. The roughness was assumed to consist of isosceles triangles. Using the same method, a

thermodynamic model is developed for roughness features consisting of asymmetric triangles. Again, the drop size is 'much larger' than the size of the drop.

Two surfaces are shown in Figure 3.3 with same geometric features but different orientations. The assumptions are same as for the model in earlier chapter. The parameters used to model the surface were - Young's contact angle = 70^o, $\beta = 20^o$, $\alpha = 70^o$, P = 20 μm.

(a) (b)

Figure 3.3: Two-dimensional symmetric profiles of sawtooth with asymmetric triangular features

Since, Gibbs energy barriers play a key role in determination of advancing and receding angles, the same are plotted for both the roughness configurations, as shown in Figure 3.4 a) and b). In this study, the role of 'geometric limit' is not considered as it has been shown that the same would not affect the values of advancing and receding angles here.

As earlier, the maximum advancing and the minimum receding angles in Figure 3.4 correspond to the maximum and minimum apparent angles as determined by Shuttleworth and Bailey [8]. Also, since Wenzel factor, r [9] is same for both the profiles and hence the Wenzel angle is also the same (~64^o) and corresponds to geometric contact angle with GEB-L = GEB-S.

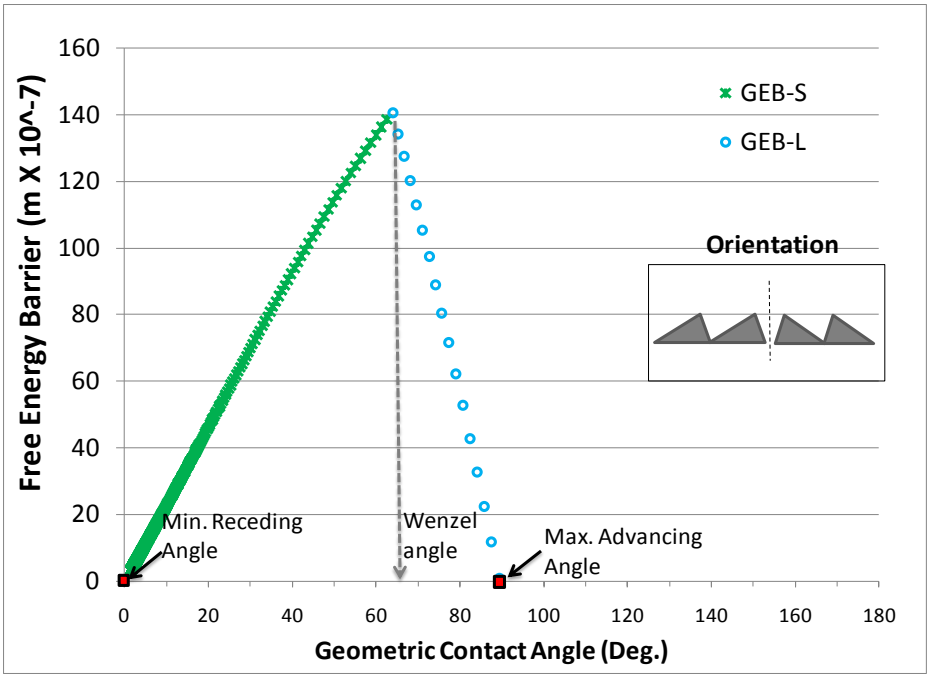

(a)

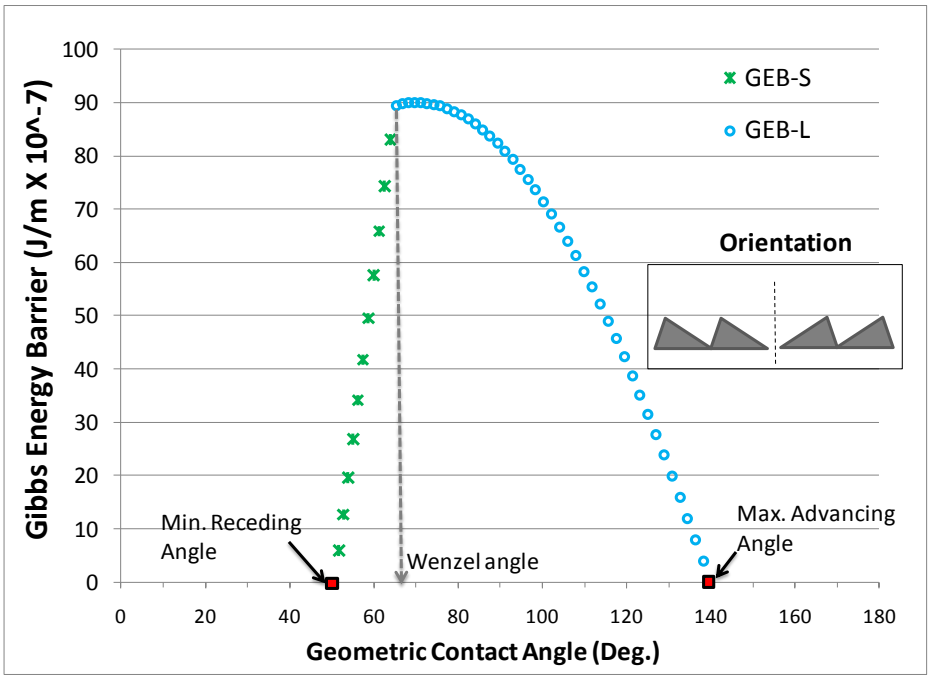

(b)

Figure 3.4: Gibbs energy barrier vs. geometric contact angle for roughness configuration shown in inset with P = 20 μm, $\alpha = 70^{o}$, $\beta = 20^{o}$ and circular 2D liquid drop with diameter ~1.4 mm with $\theta_Y = 70^{o}$

However, it is interesting to note the two surfaces have different advancing and receding angles. This result is used in the design of anisotropic surfaces in the next section.

3.3 Experiments

Simulations in the previous section demonstrated the difference in the advancing and receding angles of two similar roughness profiles with different orientations. Based upon the simulations, it is proposed that surface with an asymmetric periodic sawtooth profile would demonstrate anisotropy and the advancing and receding angles would depend upon the direction in which measurements are taken along the sawtooth.

Figure 3.5a shows the surface profile of an Echelle grating (GE1325-0875) having 79 grooves/mm and a blaze angle of 75^{o} that was purchased from THOR labs (www.thorlabs.com). The surface of the grating is coated with Alumina and has the desired asymmetric periodic sawtooth profile. As shown in the figure, a nomenclature of +ve and –ve is assumed to denote the orientation of sawtooth.

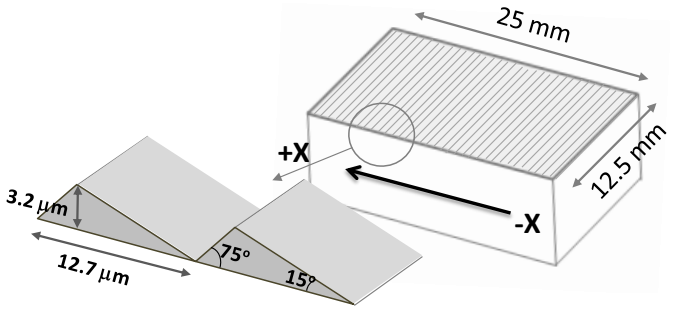

(a)

Figure 3.5: Continued on next page

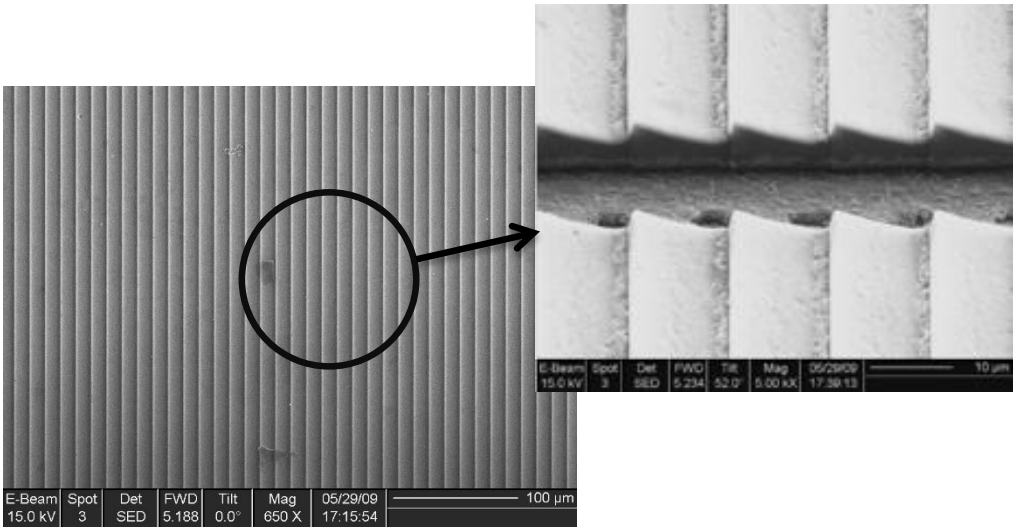

(b)

Figure 3.5: (a) Schematic of Echelle grating GE1325-0875 with 79 grooves/mm. Direction of arrow indicates orientation of sawtooth, +x and –x represent the head and tail of the arrow respectively (b) SEM image of the grating

Contact angle measurements were made using a Contact Angle System OCA 20 (DataPhysics Instruments GmbH, Germany) at 18.8 C and 40% RH. The usual contact angle variability for the measurement technique used is +/- 2°.

3.3.1 Measuring wetting anisotropy

A common method to measure the wettability of a solid surface for a given liquid is to determine the static contact angle. Researchers have used difference in static contact angle as a measure of anisotropy, specially so in the case of orthogonal anisotropy [2, 6]. However, it was shown in the earlier chapter that static contact angle of a liquid on a rough solid surface represents one of the several metastable states that the drop can exist in. Hence, static contact angle is not a good

measure of anisotropy as it is not repeatable and depends on method of drop deposition and thus should only be used as a qualitative measure of anisotropy.

Tilt angle required for sliding of drops deposited on a surface have also been used to measure anisotropy [4]. However, the critical tilt angle of a drop depends on the advancing and receding angle and the shape of contact line. The latter could be difficult to reproduce in different experiments and thus doesn't provide a repeatable method of measuring anisotropy.

In this study, advancing and receding contact angle measurements have been used to measure left-right anisotropy. The measurements have been shown to be repeatable using two different experimental methods.

3.3.2 Static contact angle measurements

As pointed out earlier, static angle measurements should only be used as a qualitative measurement of anisotropy. Here, static contact angles are measured by depositing a 3μl drop from different heights on to the surface of the grating. The measurement data is shown in Figure Figure 3.6 (a) and (b) for the parallel and perpendicular directions with respect to the sawtooth profile respectively. The different contact angles in Figure 3.6 are representative of different metastable states that the drop assumed as it was let go from different heights.

	Contact Angle (Deg.)	
Observ. #	LEFT	RIGHT
1	81.6	87.0
2	77.7	84.7
3	87.2	90.9

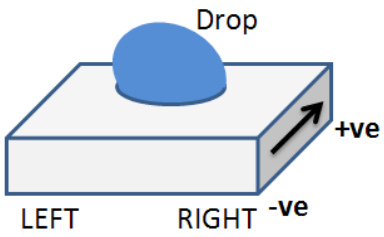

(a)

	Contact Angle (Deg.)	
Observ. #	LEFT	RIGHT
1	90.1	90.7
2	104.8	113.2
3	58.8	63.1
4	104.6	109.1

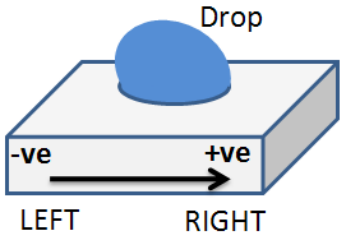

(b)

Figure 3.6: Contact angle data (a) parallel and (b) perpendicular to the sawtooth

Although, the contact angle data above doesn't show any significant anisotropy, the same is apparent when liquid is added and removed from the droplet.

As shown in Figure 3.7a, as liquid is added to the droplet, the contact line advances in only one direction and the droplet becomes asymmetric with respect to the fixed red colored reference line. Also, as the liquid is removed from the droplet, Figure 3.7b, the contact line starts receding from one end, which is different from the end where the contact line was advancing.

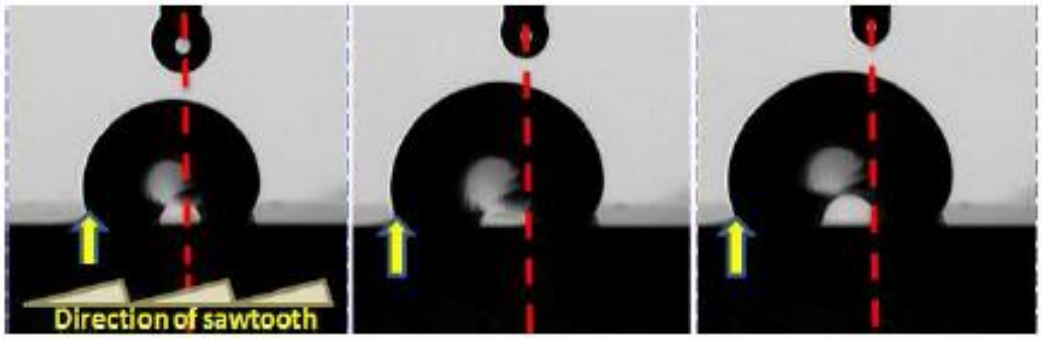

(a)

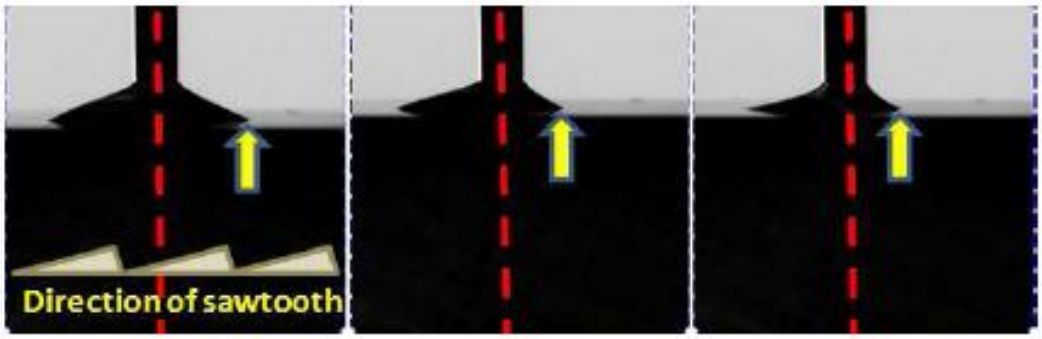

(b)

Figure 3.7: Wetting anisotropy apparent in unidirectional advance of contact line with (a) addition and (b) removal of water

3.3.3 Advancing and receding contact angle measurements

Due to wetting anisotropy, the measurement of advancing and receding contact angles was not possible in the usual manner - that is by addition and removal of liquid from the drop, as the liquid would advance and recede from only one end. Thus, two different methods were used and compared for repeatability.

A) Constant drop volume, varying tilt stage angle

In this method, the drop volume was fixed at 30 μl and the tilt stage angle was varied until the drop just started to slide and the advancing and receding angles were measured. This experiment was only done for the orientation of sawtooth shown in Figure 3.8. The measured advancing and receding angles were 89^o and 25^o respectively. This is shown in Figure 3.8, for the given orientation of the sawtooth.

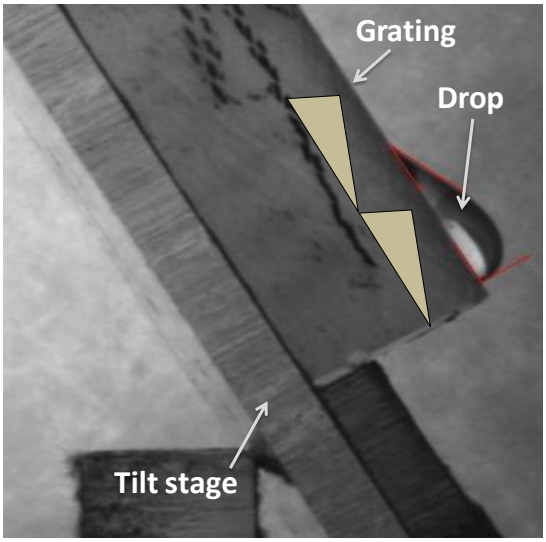

Figure 3.8: Measurement of advancing and receding angle using fixed drop volume method. Orientation of sawtooth shown in the images. Advancing angle = 87^o, Receding angle = 25^o

B) Varying drop volume, constant tilt stage angle

In the second experiment, the tilt angle of the stage was fixed and water was added to the droplet until the contact line started to move. This gave an advancing angle of 130^o and 85^o for drop sliding towards the +ve and the –ve direction respectively. The latter reading matches well with the data from fixed drop volume, varying tilt angle experiment.

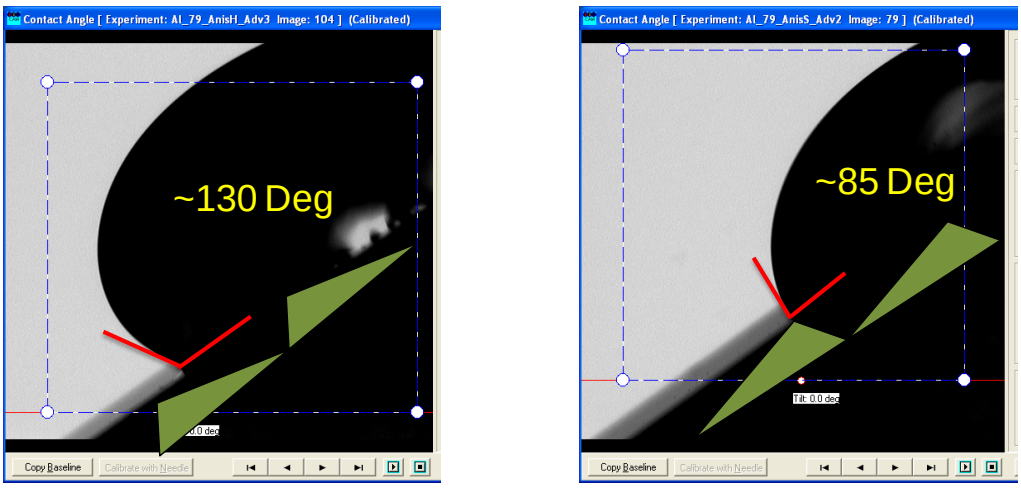

(a) (b)

Figure 3.9: Measurement of advancing angle with fixed tilt angle method. Orientation of sawtooth is shown in the images

3.4 Comparison of experiment and theory

Table 3.1 compares the advancing and receding angle measurements from the experiments and the predicted value based upon Shuttleworth and Bailey equation [8]. It should be noted that the predictions are the theoretical maximum values for the advancing and recessing angles as the vibrations haven't been taken into account. The Young's contact angle assumed for Alumina is 65^{o}.

As can be seen, the advancing angle measurements match well with the predictions. The model overestimates the receding angle measured along the direction of the arrow as shown in Figure 3.5a. This error could be due to the presence of liquid film on the surface [10].

Direction of measurement		Prediction	Data (Average of 3)
Drop moving along arrow	Advancing	140°	128°
	Receding	45°	25°
Drop moving against arrow	Advancing	80°	85°
	Receding	0°	TBD

Table 3.1: Comparison of experimental data and predictions for sawtooth profile based on [8].

Experimental error = +/- 2 Deg.

3.5 Conclusions

Thermodynamic model was developed for two asymmetric triangular roughness profiles with different orientations. The model predicted the same Wenzel angle but very different advancing and receding angles for the two profiles. This result was used to predict left-right anisotropic surface geometry which was characterized using an off-the-shelf optical grating. It was found that although the static contact angle measurements showed only minor anisotropy, the advancing and receding angle measurements revealed the wetting ratchet like characteristics of the surface. These surfaces pave the way to design smart surfaces to manipulate and control liquid motion on the same.

3.6 References

1. B. Zhao, J.S. Moore, D.J. Beebe, Science, 291 (2001) 1023.
2. D. Xia, S.R.J. Brueck, Nano Lett., 8 (2008) 2819.
3. W. Li, G. Fang, Y. Li, G. Qiao, J. Phys. Chem. B 112 (2008) 7234.
4. A. Sommers, UIUC, PhD Thesis, 2007.
5. J.Y. Chung, J.P. Youngblood, C.M. Stafford, J.Y. Chung, Soft Matter 3 (2007) 1163.
6. Yan Zhao, Qinghua Lu, Mei Li, Xin Li, Langmuir 23 (2007) 6212.
7. Kuang-Han Chu, Rong Xiao, Evelyn N. Wang, Nature Materials 9 (2010) 413
8. A. R. Shuttleworth, G. L. Bailey, J. Discuss Faraday Soc 3 (1948) 16
9. R.N. Wenzel, Ind. Eng. Chem. 28 (1936) 988
10. N. Patankar, Langmuir, 19 (2003) 1249.

4. PASSIVE CASCADABLE MICROFLUIDIC LOGIC

Surface tension based passive pumping and valving is used to design a fully cascadable microfluidic logic scheme. Using the scheme, a microfluidic equivalent of a half adder is demonstrated. Such a scheme can be used as a cheap replacement for electronic controls in microfluidic based systems e.g cheap use-and-throw diagnostic devices. They could also have applications in environments harmful to electronic controls and in space/low gravity environment.

4.1 Introduction

Microfluidic diagnostics has advanced much in the recent years with many interesting applications being explored by researchers [1-5]. However, its impact on developing countries is yet to be seen in a big way. As pointed out by Yager et al. [6], part of the reason is the fact that these devices were designed for air-conditioned labs with stable supply of power and trained personnel, which the developing countries lack. Further, portability, and low cost, amongst others, are essential design requirements for markets in the developing world which the current diagnostic systems lack.

As interfacial forces become significant at microscale, low power requirement can be obtained in microfluidic systems enabled by capillary forces. Further, since incorporation of active devices necessitate requirement of additional equipment, capillary enabled systems can offer cost savings and portability. Thus, capillary-based passive devices are very attractive candidates for design of cheap diagnostic systems.

Researchers have demonstrated capillary driven pumping schemes [7], microdispenser [8], self-fluid replacement mechanisms [9]. Further, surface and geometry modulation have enabled the design of passive microfluidic valves [10-13]. A detailed review of various passive microfluidic schemes can be found elsewhere [14]. Inspite of all these advancements, the controls for microfluidics have essentially remained electronic or pneumatic. Thus, for portability, lower cost and ease of usage, it would be desirable to integrate controls into a diagnostic microfluidic platform.

Fluid based logical devices were developed in 1950's [15] but lost to electronics as the latter scaled down in size and increased in speed. These earlier fluidic devices took advantage of the turbulent flow which is not accessible at smaller scale as the viscous forces dominate. Therefore, a completely different approach is required to design control elements for microfluidic systems.

Several researchers have attempted to design logical elements using microfluidic systems. Vestad et al. [16] demonstrated microfluidic on-chip logic operations (And, Or, Xor, Nand and Not) by using laminar flow to achieve a nonlinear system functional response. However, their device could not be cascaded as it used two different fluids streams. Using immiscible liquids, Prakash et. al [17] invented 'bubble logic' and demonstrated universal Boolean logic, bistability and numerous other traits associated with a scalable logic family. In other works, multiphase flow [18], pneumatics [19] and chemical reactions [20] have been used to demonstrate microfluidic logic and memory elements. However the systems either required active elements or could not be cascaded.

Passive liquid-liquid triggered valve which acts as an AND gate has been successfully demonstrated [10-13, 21, 22], but it lacks the functionality required for a complete control system. Passive droplet based logic devices have been designed by Toepke et al.[23] and although the design can be cascaded, an external pipeting system is required for automation which compromises portability. Thus, the development of a cascadable passive microfluidic logic is required which can be easily scaled

In this work, a scalable design scheme for passive cascadable microfluidic logic is proposed and a passive microfluidic half adder is demonstrated.

4.2 Theory and Results

A sudden expansion in flow cross-section can stop a liquid stream driven by interfacial forces [10-13, 21, 22]. Using the same basic principle, a channel geometry shown in Figure 4.1 is modeled and studied. For sake of simplicity, the channel is designed so that inputs A and B are geometrically similar. Liquid is introduced into one of the inlet channels and is driven by capillary force to the channel junction, where it encounters a sudden expansion in cross-sectional area. Based on the channel geometry and dimensions, the liquid either stops or jumps the junction to flow to the outlet. If the liquid happens to stop and liquid is introduced into the other input channel too, the meniscus meet at the junction and again, depending on channel dimensions, liquid can either stop or jumps the junction to reach the outlet. The possibilities are summarized in the Truth Table in Figure 4.1 and represent various logic gates i.e. AND [10-13,

21, 22], OR and STOP valve. The 0s and 1s, in the Figure, represent the presence and absence of liquid in a given Inlet/Outlet.

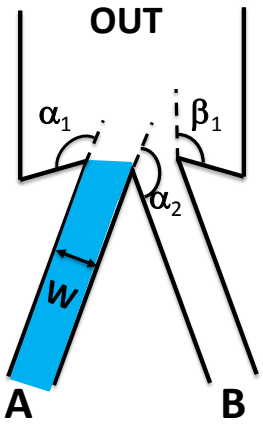

A	B	OUT		
		AND	OR	STOP
0	0	0	0	0
1	0	0	1	0
0	1	0	1	0
1	1	1	1	0

Truth Table

Figure 4.1: Schematic of channel geometry and the truth table for different possible output scenarios (W – Width of inlet channels, H – Depth of the device: not shown, α, β – geometric expansion angle)

4.2.1 AND and OR gates

For a static liquid-meniscus stopped at a sudden expansion shown in Figure 4.1, the pressure required to break the same can be calculated using the Young's equation [24] –

$$\Delta P_A = -\rho g * H - \gamma * [H * \cos(\theta_a + \alpha_1) + H * \cos(\theta_a + \alpha_2) + 2 * W * \cos(\theta_a)] / (W * H)$$

Where, θ_a is the advancing contact angle of liquid on substrate and the maximum value of $(\theta_a+\alpha_1)$ and $(\theta_a+\alpha_2)$ is π. The latter condition ensures correct calculation of the maximum break pressure. The second term on the left hand side of the equation accounts for the maximum

pressure on the meniscus due to the weight of the liquid. This contribution can be neglected for channels smaller than capillary length, l_o = sqrt($\gamma/\rho g$), which is ~2 mm for water at 25^{o}C, 50% RH with g = 9.8m/s^2. Since the dimensions of liquid channels in this study are smaller than the capillary length, gravity term is neglected. Also, it is assumed that no other body force (e.g. magnetic) is acting on the meniscus. Non-dimensionalizing the above equation gives -

$$"DP-INLET-A" = \Delta P_{non\dim\_A} = (\Delta P_A * W)/\gamma$$
$$= -[\cos(\theta_a + \alpha_1) + \cos(\theta_a + \alpha_2) + (W/H) * \cos(\theta_a)] \quad <4.1>$$

Equation 1 represents the non-dimensionalized break pressure for a single channel. However, if the liquid is present in both the channels – A and B, the break pressure can be calculated as –

$$\Delta P_{A-B} = -\rho g * H - \gamma * [2 * H * \cos(\theta_a + \beta_1) + 2 * W * \cos(\theta_a)]/(W * H)$$

In the above equation, β_1 is that expansion angle that the liquid meniscus is subjected to after streams from inlets A and B combine. As explained earlier, max.[(θ_a+β_1)]= π. Again, it is assumed that no other body force acts on the system. Non-dimensionalizing the equation and neglecting gravity (system assumed to smaller than capillary length) -

$$"DP-INLET-A-B" = \Delta P_{non\dim\_A-B} = (\Delta P_{A-B} * W)/\gamma$$
$$= -[2 * \cos(\theta_a + \beta_1) + 2 * (W/H) * \cos(\theta_a)] \quad <4.2>$$

Figure 4.2 shows the plot of break pressure for single and two channels for varying W/H. If the break pressure is positive, the liquid in the channel is not stopped by the sudden expansion and flows to the outlet and vice versa.

Three regimes of operation can be chalked out from Figure 4.2. For the first regime, the break pressure is negative for both single and combined channels. Thus the liquid can't pass the sudden expansion junction and the same acts as a STOP valve. It is easy to see that the STOP valve can function as a microfluidic diode, since it would allow liquid to flow through if the liquid approached the junction from the side labeled as OUT but not when the liquid approached the junction from channels A and/or B.

In the second regime, the break pressure is negative when the liquid is present in a single channel but it is positive when the liquid is present in both the channels. Thus the system acts as an AND Gate (Figure 4.1). In the third regime, the sudden expansion is not able to stop the liquid and the system acts as a OR Gate (Figure 4.1).

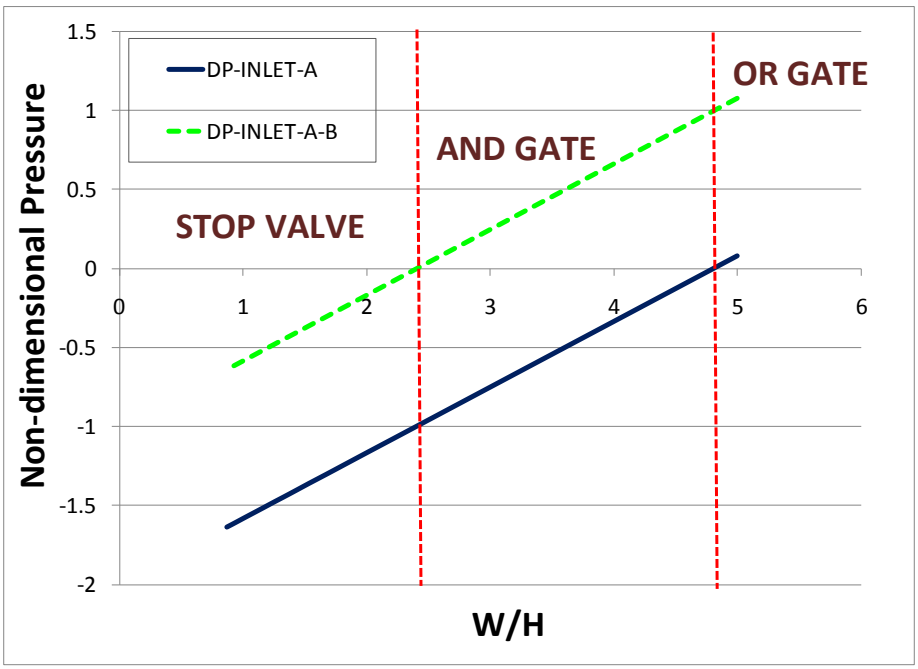

Figure 4.2 Break pressure for varying W/H (W=500μm, θ_A=78^o, α_1=110^o, α_2=140^o, β_1= 90^o, γ = 0.072 N/m)

From Figure 4.2, it can be concluded that the channel junction, shown in Figure 4.1, can function as both AND and OR gate depending on the device depth or channel width. For ease of manufacturing and to realize a cascadable system design, it is desired that the device depth of AND gate and OR gate be the same. Thus, OR gate is designed as shown in Figure 4.3, wherein each input ANDs onto itself thereby allowing liquid to reach output when any or both the channels contain liquid (or any or both the inputs are 1).

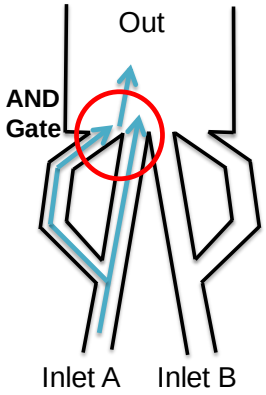

Figure 4.3 Alternative scheme for OR gate wherein each input ANDs onto itself

Figure 4.4 shows the operation of AND gate. PMMA was used as the device substrate, since it is naturally hydrophilic ($\theta_A = 78^o$), and the liquid was de-ionized water colored with red food dye. The width of input channels was 500 μm, the depth of the device was 300 μm and the expansion angles ($\alpha_1 = \alpha_2$) at the junction were 150^o. With these dimensions, the calculated break pressure of a single channel was -188 Pa and -44 Pa for both the channels. Here, the break pressure for both the channels in negative, contrary to what is shown in Figure 4.2. However, the drop placed at the inlet has a net positive pressure of around 100 Pa, which counters this negative pressure and allows for AND gate functioning. As can be seen from the figure, water is allowed to the outlet only when both the channels have water present (both the inputs are 1).

Figure 4.5 shows operation of OR Gate. The parameters and materials used in the design of OR gate were the same as the AND gate and the calculated break pressure for single input, which ANDs onto itself, was –44 Pa. This negative pressure was again countered by the positive pressure due to the drop present at the inlet. As can be seen, the water moves to the output once it is introduced in one of the inputs.

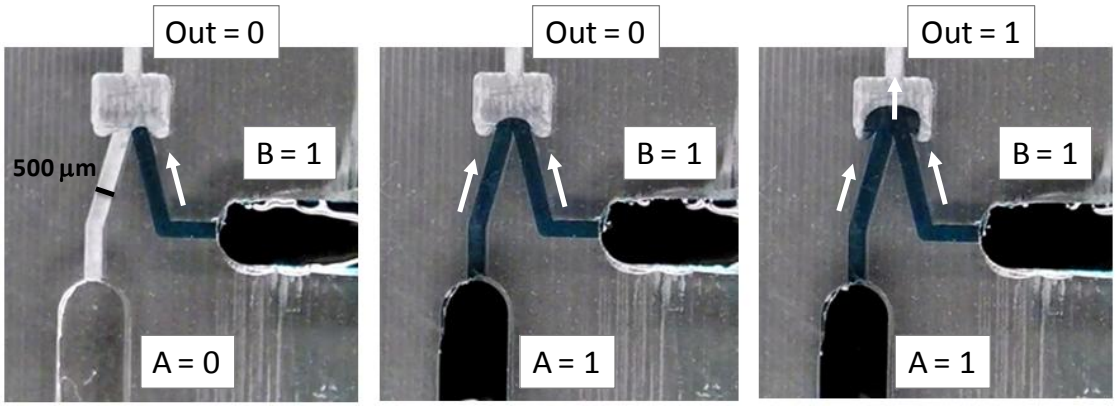

(a) (b) (c)

Figure 4.4: Operation of AND gate with inputs A and B. Channel width at thinnest section = 500 µm, $\alpha_1 = \alpha_2 = 150^o$, device depth = 300 µm

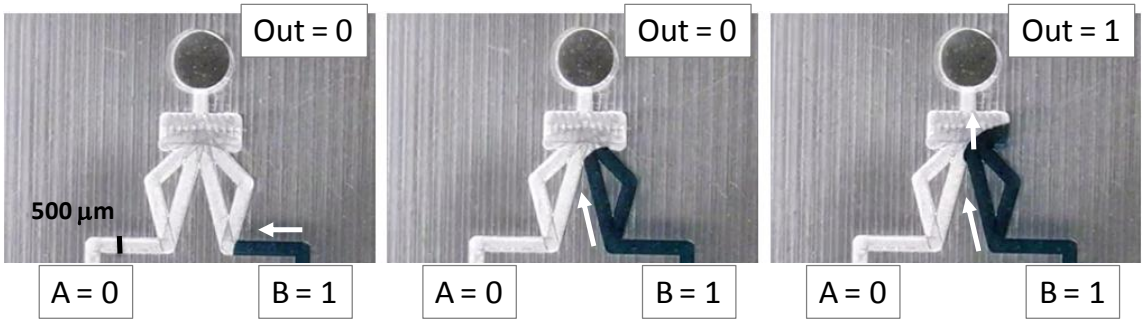

(a) (b) (c)

Figure 4.5: Operation of OR gate at the junction of inputs 1 and 2. Device depth = 300 µm.

It should be noted that equations 4.1 and 4.2 have been quantitatively validated by various researchers [22, 25 - 28] for several different substrate and liquid combinations. Further, since the scope of the work is limited to qualitaive validation of logic scheme, only the same is demonstrated here.

4.2.2 NOT Gate

All the logic functions can be generated using a NAND gate [29], therefore, along with an AND gate, it is usually necessary to design a NOT gate. A version of NOT gate was designed by Beebe et al. [30]. Their scheme is shown in Figure 4.6a and the channels have been relabeled to demonstrate a NOT gate function. It can be seen from the figure that when input channel has fluid, that is input = 1, the hydrogel expands and blocks the reservoir channel. Therefore, when liquid is added to reservoir channel, it doesn't reach the output and thus output = 0. Further, if there is no liquid in the input channel, input = 0, the liquid added to the reservoir channel reaches the output. Thus the system acts as a NOT gate as also shown by the truth table in Figure 4.6b.

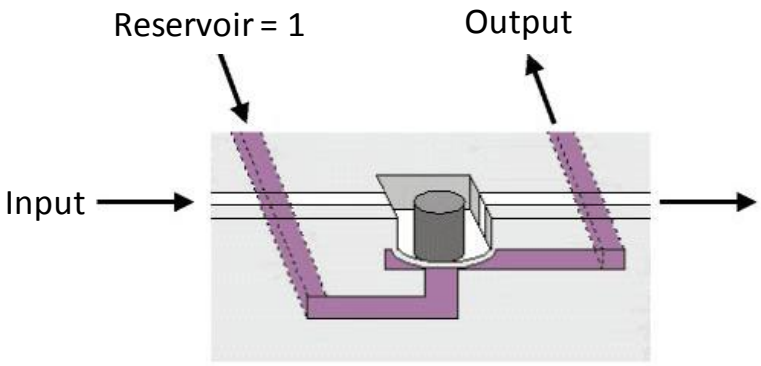

(a)

Input	Reservoir	Output
0	1	1
1	1	0

(b)

Figure 4.6 a) NOT gate design using hydrogel [30] b) Truth Table for NOT gate

However, such a scheme requires addition of liquid to the reservoir only after the input state has been determined. Thereby, cascading such a scheme would not only be time consuming, due to the slow acting hydrogels, but would also be difficult to completely automate.

In the next section I suggest a scheme for a cascadable logic device by removing all NOT gates at the expense of increasing the number of input channels at each logic operation.

4.2.3 Cascadable logic scheme

An alternative design of NAND gate is shown in Figure 4.7. It can be seen that an OR gate can be used to create a NAND gate, given that complimentary of the inputs are available. Further, an AND and a NAND output can form a complimentary set of inputs for the next level of computation.

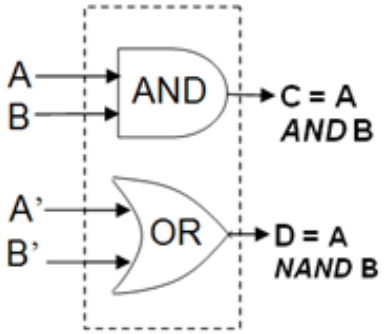

A	B	A'	B'	A AND B	A' OR B'
0	0	1	1	0	1
0	1	1	0	0	1
1	0	0	1	0	1
1	1	0	0	1	0

Figure 4.7 NAND Gate

Thus, since a complimentary set of inputs provided at the first level of computation can generate a NAND gate, they can thus be used to generate all possible logic operations. Thereby, complimentary outputs are generated after each logic operation, which then form a complimentary set of input to the next level of computation, thereby allowing cascading. This generalized scheme is demonstrated in Figure 4.8.

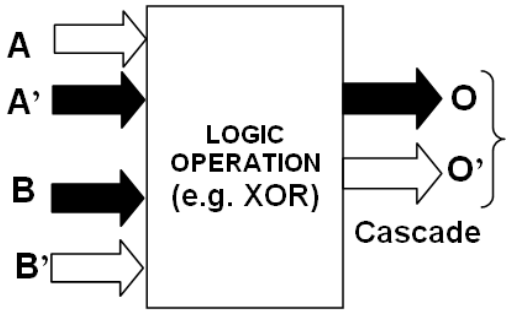

Figure 4.8 Complimentary inputs can generate complimentary outputs for a cascadable logic system

The first stage of complimentary inputs can be generated in several ways including manual input and hydrogel response [30] based on physical or chemical stimulus from the environment e.g. pH [31, 32], temperature [33, 34], light [35], pressure [36], biological agents [37] etc.

Although this scheme does double the number of inputs and outputs at each level so that the number of operations to be performed for N stages of computation would increase by a multiple of 2^N. But, in a practical situation, one would only generate output and its complimentary only if they are needed for further operations.

Next, a half-adder is demonstrated and microfluidic binary addition is shown using the scheme described above.

4.3 Passive Microfluidic Half Adder

As an example of the above explained scheme, an electronic equivalent of half adder is realized. A half adder can perform binary additions and the truth table of the same is shown in Figure 4.9.

		Half Adder	
A	B	CARRY	SUM
0	0	0	0
0	1	0	1
1	0	0	1
1	1	1	0

Figure 4.9 Truth Table for Half adder

As can be seen, half adder consists of a 'Carry', which is an AND gate, and a 'Sum', which is a XOR gate. Since the function of AND gate and NAND gate has been demonstrated in previous section, this section will focus on generating a XOR gate and its complimentary, XOR'. Further, only a two input system is demonstrated here and a multiple input system can be designed in a similar manner.

A XOR Gate for a two input system can be expressed as –

(A **AND** B') **OR** (A' **AND** B) = A **XOR** B

And, the complimentary XOR' as –

(A **AND** B) **OR** (A' **AND** B') = A **XOR'** B

Since, both XOR and XOR' use the same logic operations, they can be derived from the same channel geometry by interchanging inputs. This can be seen in Figure 4.10. If the inputs 1, 2, 3 and 4 are assigned A, B', A' and B respectively, it results in a XOR Gate. Also, when the same inputs are assigned A, B, A' and B' respectively, the output is a XOR'.

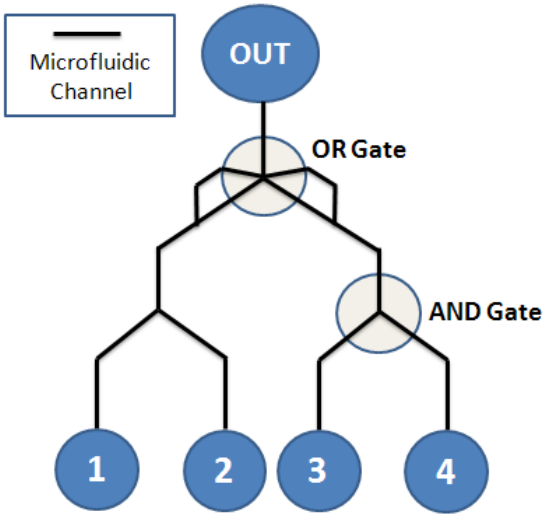

1	2	3	4	OUT
A	B'	A'	B	XOR
A	B	A'	B'	XOR'

Figure 4.10: Channel scheme for XOR and XOR'

The fabricated device is shown in Figure 4.11, and the functioning of the device is demonstrated for inputs A and B where A = 0 and B = 1 and thus output, Out = 1. The dimensions for the AND

and OR gates in the XOR/XOR' device is exactly the same as used earlier for AND and OR gates demonstrated in Figures 4.4 and 4.5.

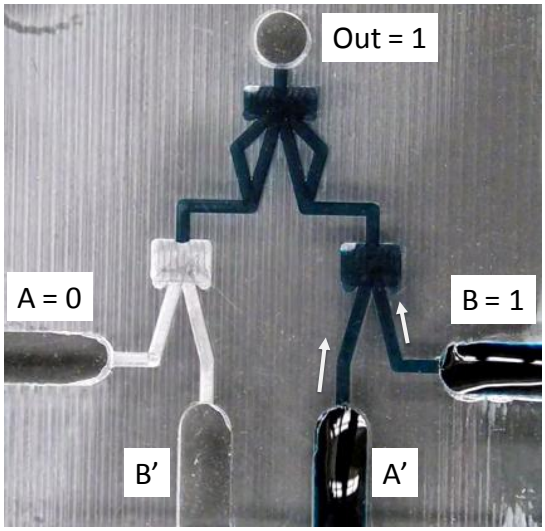

Figure 4.11: XOR gate. Channel width at thinnest section = 500 μm, $\alpha_1 = \alpha_2 = 150^o$, device depth = 300 μm

4.4 Scalable and cascadable logic scheme

In the demonstrated scheme for XOR gate (Figure 4.11), A=0 and B=1 and hence, channels labeled A' and B contain liquid. If multiple and/or simultaneous logic operations are to be performed, the liquid in channels A' and B need to be transferred to different parts of the device. Thus to ensure scalability, a multi-layer channel scheme with passive and controlled transfer of liquid between the layers is required.

Such a scheme has been created by using the concept of liquid-wall, which has been demonstrated earlier by Malik et al. [38]. The details of the scheme are presented in chapter 5

and a schematic of the transfer channels is shown in Figure 4.12. In the figure, two criss-crossing channels, 1 and 2, are shown with channel 1 containing liquid. It can be seen that channel 1 is in bottom part or substrate and channel 2 is in the top part or cover of the device. As the liquid flows in channel 1, it forms a liquid-wall at the junction where the channels criss-cross. By controlling the dimensions of the liquid-wall at the junction, the flow of liquid from channel 1 to channel 2 can be controlled. In Figure 4.12a, the dimensions of the liquid wall don't allow the flow from channel 1 to channel 2 while in Figure 4.12b, the liquid from channel 1 flows into channel 2.

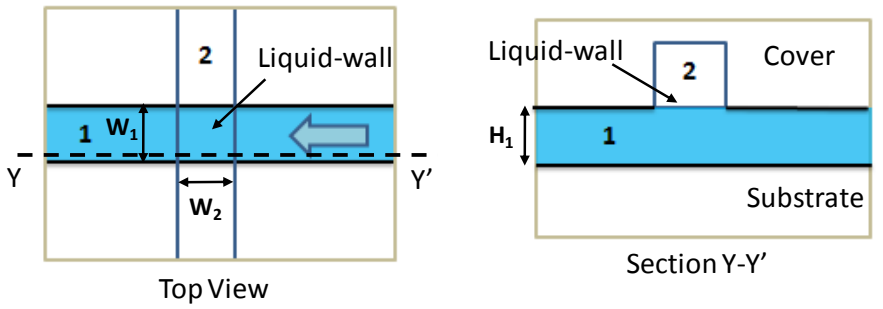

(a)

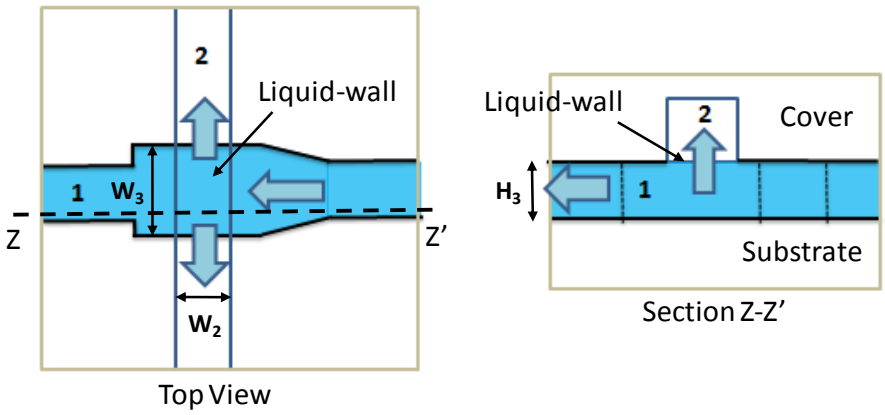

(b)

Figure 4.12: Crisscrossing channels with liquid-wall between them a) No flow of liquid from channel 1 to 2 b) Liquid flows from channel 1 to 2 ($W_1 = W_2 = 500$ μm, $W_3 = 1600$ μm, $H_1 = H_3 = 1000$ μm)

Using transfer channels, XOR and XOR' functions are simultaneously demonstrated in Figure 4.13. As can be seen, liquid is transferred across different channels to the destination channel and complimentary logic operations are performed simultaneously.

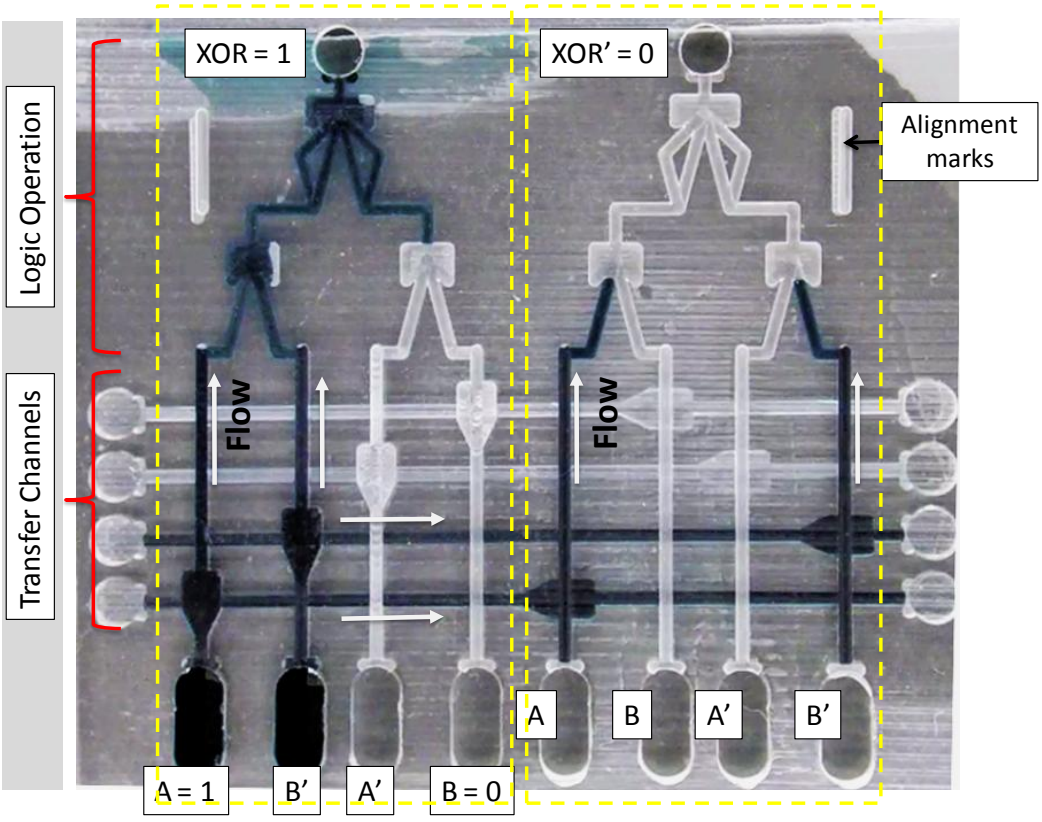

Figure 4.13: XOR and XOR' obtained simultaneously using transfer channel for inputs A=1, B=0. Channel width at thinnest section = 500μm, Transfer Channel section depth = 1000μm, Logic Operation section channel depth = 300μm. Other dimensions as described in Chapter 5.

Thus, using the logic scheme described and transfer channels, any logic operation and any number of operations can be performed.

4.5 Methods

In our study, PMMA ($\theta_A = 78^o, \theta_R = 48^o$ with DI water) was used as the substrate and DI water was used as the liquid. PMMA pieces were cut and fixed on Microlution's micro milling machine. Inlet and outlet holes were drilled using PMT's (www.pmtnow.com) 2mm endmill (TS-2-0400-S). Thereafter, the pieces were planarized and channels were machined using a 500 micrometer endmill (TS-2-0200-S) using a G-code specifically written for the channel design.

The machining parameters were chosen so as to ensure that the maximum to minimum variation in depth of the channel was ~2 micrometer. This criterion was chosen arbitrary but it ensured that the capillary driven fluid flow inside the channel did not pin due to machining marks. The final machining parameters were RPM = 8000, feed = 50mm/min and step over =0.25 mm. The devices were bonded using an in house adhesive bonding process developed at the MNMS cleanroom. Minimal alignment was required during the bonding process as the top plate didn't require machining. During the bonding process, the PMMA pieces were first cleaned with DI water and ethanol. Adhesive (D75) was applied using a PDMS puck, which was pre-coated with adhesion promoter (VM752). Thereafter, the devices were bonded in a thermal bonder using the following process – 1) Press. = 1MPa, Temp = 105 C for 5 min 2) Press. = 1MPa , Cool to 50 C, 1hr.

The fabricated XOR and XOR' gate with transfer channels (Figure 13) was around 40mm X 40mm in dimension and represented the geometric limit of the microlution machine. More complicated logic operations can be accomodated using a smaller end mill or via other fabrication methods like hot embossing [39, 40].

It should be noted that any hydrophilic material can't be used as a substrate, especially with channels of rectangular cross-section, because if the contact angle of the substrate is below 45^{o}, the edge of the cross section is significantly wetted thereby eliminating the capillary pressure barrier [41].

4.6 Conclusions

A scalable and cascadable passive microfluidic logic scheme has been designed and a half adder (AND and XOR gates) was demonstrated using the proposed scheme. Further, using liquid-walls, a passive 'transfer channel' scheme is also designed to transport liquid across the microfluidic chip.

In the logic scheme, no NOT gate is required in such a scheme as complimentary inputs are provided at the first level of computation and complimentary outputs generated thereafter are used for cascading. Although this scheme doubles the number of inputs and outputs at each level but in a practical scenario, one would only generate output and its complimentary only if they are needed in further logic operations. The first stage of complimentary inputs can be

generated in several ways including manual input and hydrogel response [30] based on physical or chemical stimulus from the environment e.g. pH [31,32], temperature [33, 34], light [35], pressure [36], biological agents [37] etc. Thus the microfluidic logic scheme could possibly sense the environmental stimulus and perform logical operations accordingly thereby acting as a Central Processing Unit (CPU) to perform computations for a passive or an active device. The output from the logic scheme could be used to further trigger a process e.g. a hydrogel based valve which controls a chemical reaction. Thus, such a system could bring cheap computing to diagnostic devices, microfluidic lab-on-chip system, microassays and related technologies. Also, in environment corrosive to silicon electronics, microfluidic logic could provide a cheap replacement, although, they can by no means match the speed of the former.

In its current form, the passive logic device has low robustness to liquid contamination. Thus the logic scheme would have to be isolated from the external environment possibly using hydrogels as a communication medium both for input and output. Also, since the device is passive, it would need to be flushed after one use. This limitation could be overcome by using a volatile liquid or liquid evaporation by changing device temperature.

4.7 References

1. J. Moorthy, G. A. Mensing, D. Kim, S. Mohanty, D. T. Eddington, W. H. Tepp, E. A. Johnson, D. J. Beebe, Electrophoresis 25 (2004) 1705.

2. C.J. Easley, J. M. Karlinsey, J.M. Bienvenue, L.A. Legendre, M.G. Roper, S.H. Feldman, M.A. Hughes, E. L. Hewlett, T. J. Merkel, J. P. Ferrance, J. P. Landers, Proc. Natl. Acad. Sci. 103 (2006) 19272.
3. M.A. Burns, B.N. Johnson, S.N. Brahmasandra, K. Handique, J.R. Webster, M. Krishnan, T. Sammarco, P.M. Man, D. Jones, D. Heldsinger, C.H. Mastrangelo, D.T. Burke, Science 282 (1998) 484.
4. R.H. Liu, M.J. Lodes, T. Nguyen, T. Siuda, M. Slota, H.S. Fuji, A. McShea, Anal. Chem. 78 (2006) 4184.
5. K. Sato and T. Kitamori, J. Nanosci. Nanotechnol. 4 (2004) 575.
6. P. Yager, T. Edwards, E. Fu, K. Helton, K. Nelson, M.R. Tam, B.H. Weigl, Nature 442 (2006) 412
7. M. Zimmermann, H. Schmid, P. Hunziker, E. Delamarche, Lab Chip 7 (2007) 119
8. A. Puntambekar, J.W. Choi, C.H. Ahn, S. Kim, V. Makhijani, Lab Chip 2 (2002) 213.
9. K.H. Chung, J.W. Hong, D.S. Lee, H.C. Yoon, Analytica Chimica Acta, 585 (2007) 1.
10. Y. Feng, Z. Zhou, X. Ye, J. Xiong, Sensors and Actuators A, 108 (2003) 138.
11. P.F. Man, C.H. Mastrangelo, M.A. Burns, D.T. Burke, MEMS'98 pp 45.
12. M.J. Madou, G.J. Kellogg, Proceedings of the SPIE 3259 (1998) 80
13. R.M. Moroney, MSM' 98, Santa Clara, CA, 1998 pp. 526
14. Bhushan, Bharat (Ed.), Springer Handbook of Nanotechnology 3rd ed (2010)
15. K. Foster ,G.A. Parker, Fluidics: Components and Circuits, Wiley-Interscience, New York (1970)
16. T. Vestad, D.W.M. Marr, Applied Physics Letters 84 (2004) 25.
17. M. Prakash, N. Gershenfeld, Science 315 (2007) 832

18. A. Groisman, M. Enzelberger, S.R. Quake, Science 300 (2003) 955.
19. W. H. Grover, R. H. C. Ivester, E. C. Jensen, R. A. Mathies, Lab Chip 6 (2006) 623
20. W. Zhan, R. M. Crooks, J. Am. Chem. Soc. 125, no. 33 (2003) 9934
21. J. Melin, N. Roxhed, G. Gimenez, P. Griss, W. Van der Wijngaart, G. Stemme, 12th International Conference on Transducers, Solid-State Sensors, Actuators and Microsystems 2 (2003) 1562.
22. Sung-Jin Kim, Yong Taik Lim, Haesik Yang,Yong Beom Shin, Kyuwon Kim, Dae-Sik Lee, Se Ho Park, Youn Tae Kim., Analytical Chemistry 77, no. 19 (2005) 6494.
23. M. W. Toepke, V. V. Abhyankar, D. J. Beebe, Lab Chip 7 (2007) 1449.
24. T. Young, G. Peacock, editor. Miscellaneous works, London' J. Murray, Vol. 1, 1855.
25. Jun Zeng, Manish Deshpande, Ken B. Greiner, John R. Gilbert, ASME 2000.
26. Jerry M. Chen, Po-Chun Huang, Mou-Gee Lin, Microfluid Nanofluid 4 (2008) 427.
27. Jerry M. Chen, Chun-Yi Chen, Chia-Hung Liu, Jap. J. Applied Physics 47, no. 3, (2008) 1683.
28. Hansang Cho, Ho-Young Kimb, Ji Yoon Kang, Tae Song Kim, J. Colloid and Interface Science 306 (2007) 379.
29. Mano/Kime, Logic and Computer Design Fundamentals, Prentice-Hall Inc.,2nd ed (2001)
30. D. J. Beebe, J.S. Moore, J.M. Bauer, Q. Yu, R.H. Liu, C. Devadoss, B.H. Jo, Nature 404 (2000) 588.
31. D.T. Eddington, D.J. Beebe, Adv. Drug Del. Rev. 56, no. 2 (2004) 199.
32. D.T. Eddington, D.J. Beebe, J. Microelectromech. Syst., 13 (2004) 586.
33. A. Richter, D. Kuckling, S. Howitz, T. Gehring, K-F. Arndt, J. Microelectromech. Syst., 12 (2003) 748.

34. H. J. Van der Linden, W. Othuis, P. Bergveld, Lab Chip, 4 (2004) 619.

35. A. Suzuki, T. Tanaka, Nature, 346 (1990) 345.

36. K.K. Lee, E.L. Cussler, M. Marchetti, M.A. McHugh, Chem. Eng. Sc. 45 (1990) 766.

37. T. Miyata, N. Asami , T.A. Uragami, Nature 399 (1999) 766.

38. T. Malik, N.X. Fang, "Flow Inside Microchannels With Liquid-Walls", ASME Conf. Proc. 921 (2008), DOI:10.1115/IMECE2008-67546

39. T. Koerner,L. Brown, R. Xie, R.D. Oleschuk, Sensors and Actuators B 107 (2005) 632.

40. L.J.Kricka,P. Fortina, N.J. Panaro, P. Wilding, G. Alonso-Amigoc, H. Becker, Lab on a Chip 2 (2002) 1.

41. E. Kim, G.M.J. Whitesides, Phys. Chem. B. 101 (1997) 855.

5. WALL-LESS FLOW IN MICROCHANNELS

Microfluidic flows are characterized by high surface-area to volume ratio resulting in dominant interfacial-forces. Many researchers have used this to their advantage and designed microfluidic pumping systems [1], self-fluid replacement mechanisms [2] etc. Further, surface and geometry modulation have extended the capability to exploit these effects to design microfluidic valves [3,4,5,6].

Recently, selective surface patterning has been used to confine microfluidic flow using only two physical walls [7]. Although, such a system offers the ability to define hydrophobic/hydrophilic pathways with varying shapes, dynamic manipulation of pathways is not possible. Also, the advancing contact angle of the liquid on the hydrophobic region limits the maximum pressure that the 'liquid-walls' can sustain and the hydrophobic/hydrophilic pathways can be washed away over time. This constraints the use of these systems at microscale.

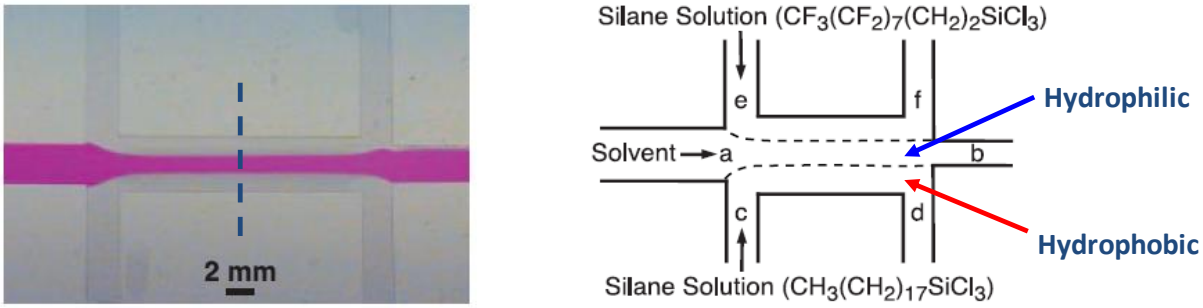

(a) (b)

Figure 5.1: Liquid-wall using selective chemical patterning a) Liquid in microfluidic channel with only two physical walls b) Chemical patterning used for a) [7]

In this study, liquid-wall is created on hydrophilic substrate by using geometric modulation and without the need for hydrophobic patterning. A theoretical model has been developed to calculate the channel geometry required to create a liquid-wall. Thereby, a microfluidic channel is fabricated and liquid-wall flow is demonstrated. This scheme is used in designing 'transfer-channels' to passively control the transfer of liquid in a multi-layered microfluidic device. The 'transfer-channels' are thereby used to add scalability to passive liquid-logic, demonstrated in previous chapter. The scheme can be also be used in liquid-gas chemical reactors, passive microfluidic valves, microfluidic pressure switches and in eliminating air entrapment issues.

5.1 Theory

A sudden expansion in flow cross-section can stop a liquid stream driven by capillary force and this principle has been used to design passive microfluidic AND gate [3,5,6,8,9]. Using the same basic principle, I demonstrate the creation of liquid-wall using a channel design shown in Figure 5.2.

As can be seen, two hydrophilic substrates are bonded together to form the microfluidic channels. The bottom plate has two channels, where the depth of one is more than the other. As the liquid is introduced in the shallower channel, it is driven by capillary force. This flowing liquid then encounters a sudden difference in the depth perpendicular to the flow direction. If properly dimensioned, the liquid forms a meniscus which stops it from spilling into the deeper channel thereby creating a liquid-wall. The liquid-wall can also sustain a pressure driven flow until the pressure is below a critical value.

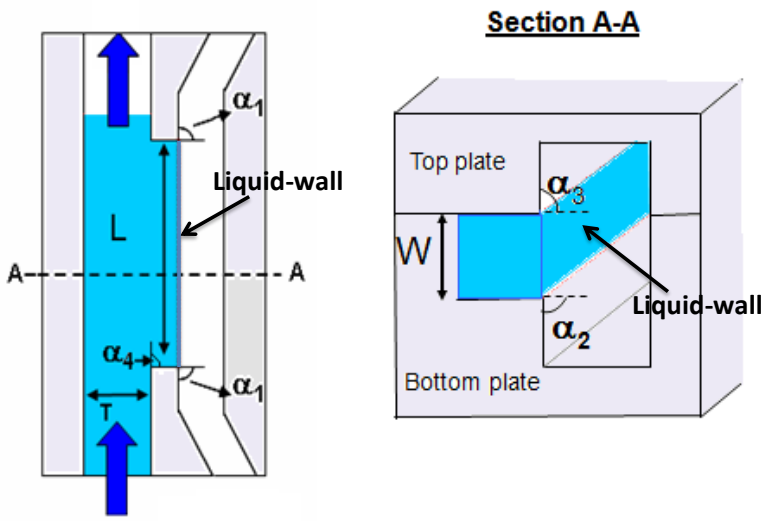

Figure 5.2: a) Schematic of channel geometry for liquid-wall flow (L – length of liquid wall, W-height of liquid-wall, α – expansion angle, T – width of inflow channel)

For a static liquid-wall, the pressure required to break the same can be calculated by using Young's equation [10] –

$$\Delta P_{break} + \rho g * W = -\gamma * [2W * \cos(\theta_a + \alpha_1) + L * \cos(\theta_a + \alpha_2) + L * \cos(\theta_a + \alpha_3)] / W * L \quad \text{<5.1>}$$

Where, Max.$[(\theta_a+\alpha_1)]$, Max.$[(\theta_a+\alpha_2)]$, Max.$[(\theta_a+\alpha_3)]$ = 180^o, θ_a is the advancing contact angle of the liquid on solid substrate, γ is the surface tension of the liquid, ρ and g are liquid density and acceleration due to gravity respectively. It can be seen that the depth of the deeper channel isn't one of the design parameters and can be chosen arbitrarily. The second term on the left hand side of the equation accounts for the maximum pressure on the liquid-wall due to the weight of the liquid. This contribution can be neglected for sub-millimeter deep channels.

Neglecting liquid weight and non-dimensionalizing equation 5.1 –

$$-\frac{\Delta P_{break} * W}{\gamma} = 2(W/L) * \cos(\theta_a + \alpha_1) + \cos(\theta_a + \alpha_2) + \cos(\theta_a + \alpha_3) \quad \text{<5.2>}$$

Figure 5.3 shows the plot of break pressure for different depths of the shallower channel and different lengths of the liquid-wall. The liquid assumed is water and the substrate assumed is Polymethylmethacrylate or PMMA (θ_a = 78° with DI water). The parameters used for the graph were α_1 = 90°, α_2 = 90°, α_3 = 0°, α_4 = 90° and width, T = 500μm.

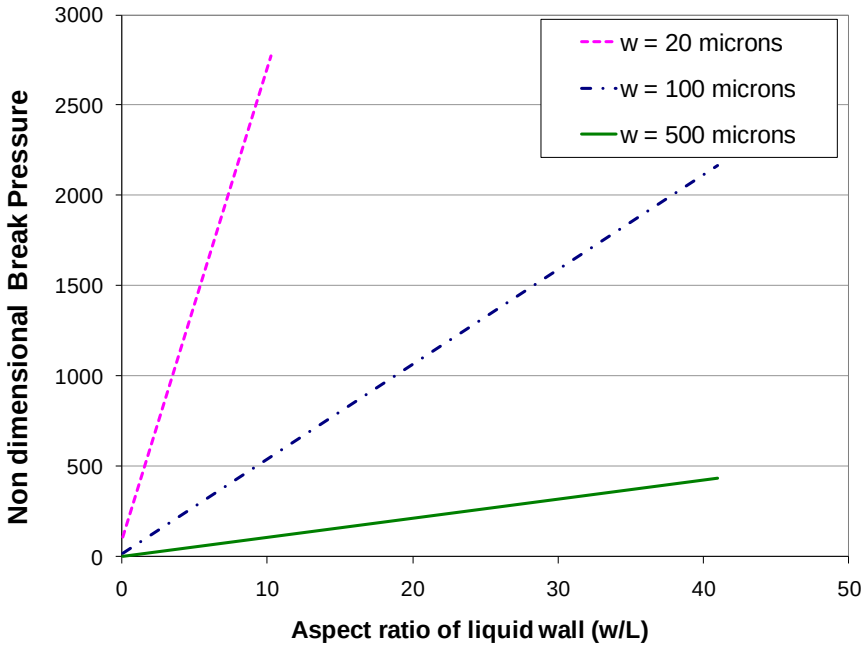

Figure 5.3: Break pressure for different dimensions of the liquid wall with varying aspect ratio (α_1 = 90°, α_2 = 90°, α_3 = 0°, α_4 = 90° and width, T = 500μm). Refer Figure 5.2

It should be noted that equations 5.2 has been quantitatively validated by various researchers [11 - 14] for several different substrate and liquid combinations. Further, since the scope of the work is limited to qualitaive validation of liquid-wall, only the same is demonstrated

here.

In case of a pressure driven flow, the break pressure of the liquid-wall determines the maximum length of the flow channel, for a given flow rate . This is because the pressure drop is a function of flow rate and flow resistance. For a constant flow rate, the flow resistance keeps increasing as the liquid fills the microfluidic channel and thus the inlet pressure must be increased accordingly. Thus, since the break pressure is constant, as the flow length increases, the liquid-wall breaks. For a capillary driven flow, since inlet pressure is constant, the flow rate automatically adjusts to balance the pressure gradient and thus the flow length is not restricted in such a scenario.

Also, it can be seen from Figure 5.2 that as the liquid flows in and forms liquid-wall, it encounters a sudden expansion (angle α_4). Thus, it should be ensured that the liquid doesn't stop at this expansion. This can be ensured by sizing the inflow channel width, T so that the break pressure to overcome the particular sudden-expansion is negative –

$$\Delta P_{break} < 0 \; where, (\Delta P_{break})$$
$$= -\gamma * [W * \cos(\theta_a + \alpha_4) + W * \cos\theta_a + 2T * \cos\theta_a] / W * T$$

5.2 Methods

In our study, Polymethylmethacrylate or PMMA ($\theta_A = 78^o, \theta_R = 48^o$ with DI water) was used as the substrate and DI water was used as the liquid. 2X4 cm PMMA pieces were cut and fixed on Microlution's micro milling machine. Inlet and outlet holes were drilled using PMT's (www.pmtnow.com) 2mm endmill (TS-2-0400-S). Thereafter, the pieces were planarized and

channels were machined using a 500 micrometer endmill (TS-2-0200-S) using a G-code specifically written for the channel design.

The machining parameters were chosen so as to ensure that the maximum to minimum variation in depth of the channel was ~2 micrometer. This criterion was chosen arbitrary but it ensured that the capillary driven fluid flow inside the channel did not pin due to machining marks. The final machining parameters were RPM = 8000, feed = 50mm/min and step over =0.25 mm. The devices were bonded using an in house adhesive bonding process developed at the MNMS cleanroom. No alignment was required during the bonding process as the top plate didn't require machining. During the bonding process, the PMMA pieces were first cleaned with DI water and ethanol. Adhesive (D75) was applied using a PDMS puck, which was pre-coated with adhesion promoter (VM752). Thereafter, the devices were bonded in a thermal bonder using the following process – 1) Press. = 1MPa, Temp = 105 C for 5 min 2) Press. = 1MPa , Cool to 50 C, 1hr.

It should be noted that any hydrophilic material can't be used as a substrate, especially with channels of rectangular cross-section, because if the contact angle of the substrate is below 45^o, the edge of the cross section is significantly wetted thereby eliminating the capillary pressure barrier [15].

5.3 Liquid-wall demonstration

In the study, I used PMMA as our substrate and DI water was used as the liquid. The parameters used for fabrication were $\alpha_1 = 90^o$, $\alpha_2 = 90^o$, $\alpha_3 = 0^o$, $\alpha_4 = 90^o$ and width, T = 500μm. The channel length was arbitrarily chosen to be 13 mm and the device depth was calculated to be 200

μm. Figure 5.4 shows the water-wall formed after the water fills the channel. When water is introduced into the adjacent empty channel, it instantly 'switches-off' the water wall by filling the empty channel.

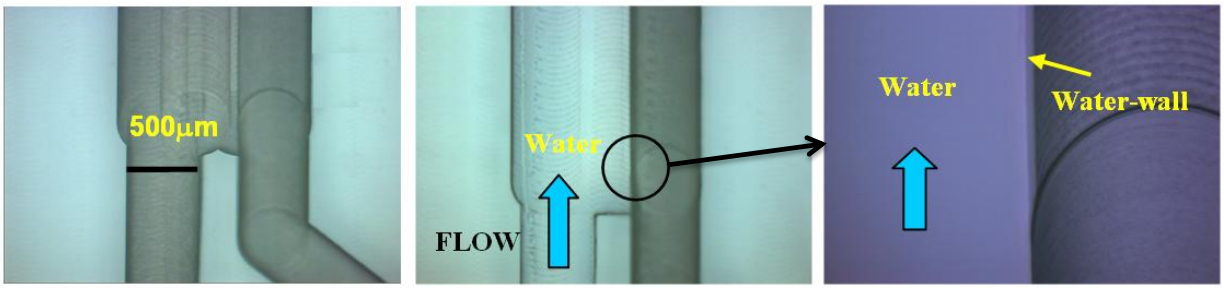

Figure 5.4: Water in the channel confined by water- wall

5.4 'Transfer-channel' design

Liquid-wall is used to design 'transfer-channels' to passively control the transfer of liquid in a multi-layered microfluidic device. This is shown in Figure 5.5, 5.6 and 5.7.

In the figure 5.5, two criss-crossing channels, 1 and 2, are shown with channel 1 containing liquid. It can be seen that channel 1 is in bottom part or substrate and channel 2 is in the top part or cover of the device, forming a two-layered microfluidic channel network. As the liquid flows in channel 1, it forms a liquid-wall at the junction where the channels criss-cross. By controlling the dimensions of the liquid-wall at the junction, the flow of liquid from channel 1 to channel 2 can be controlled.

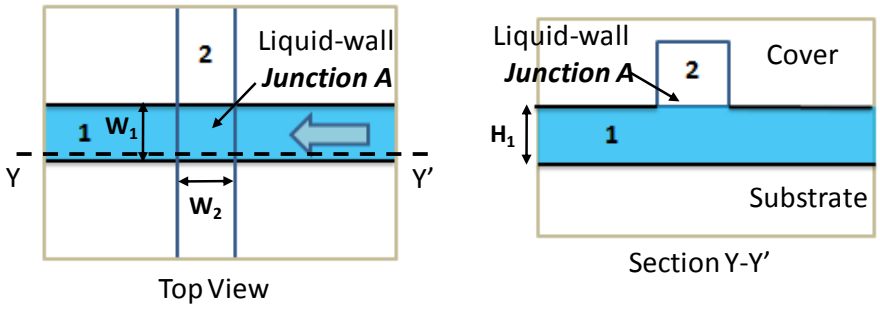

(a)

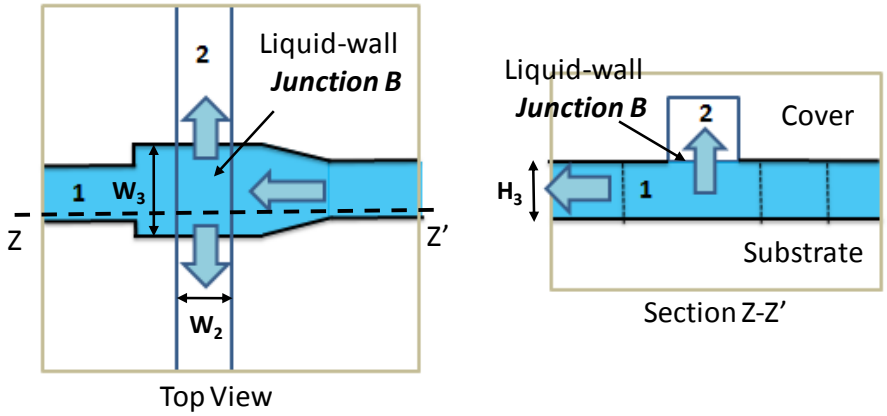

(b)

Figure 5.5: Crisscrossing channels with liquid-wall between them a) No flow of liquid from channel 1 to 2 as liquid-wall at junction A is intact b) Liquid flows from channel 1 to 2 due to breaking of liquid-wall at junction B

During the experiment, the channels were dimensioned so that:

Liquid-wall break pressure at junction A > 50 Pa > Liquid-wall break pressure at Junction B.

Here, 50 Pa represents the positive pressure due to the curvature of the liquid drop placed at the inlet. This positive pressure at inlet is used to break the liquid-wall at junction B without breaking the liquid wall at junction A, thereby allowing controlled transfer of liquid. Further, the depth of the channels 1 and 2 are so dimensioned so as to allow the formation of liquid wall at junction A and junction B. The calculations are done using equation 5.1.

The channels have been dimensioned for a combination of DI water (γ_{LA} = 0.072 N/m @ 25^{o}C) and PMMA (θ_a for DI water = 78^{o} @ 25^{o}C, 50% RH). The resultant dimensions are: $W_1 = W_2$ = 500 μm, W_3 = 1600 μm and $H_1 = H_3$ = 1000 μm. The break pressure of liquid wall at junctions A and B are shown in Table 5.1.

Junction	**Break Pressure (Pa)**
Liquid-wall Junction A	219.5
Liquid-wall Junction B	24.1

Table 5.1: Break pressure for different liquid-wall junctions

Using the criss-crossing channel scheme in Figure 5.5, a two layered microfluidic device is designed to passively control the transfer of liquid from a given inlet channel to a given outlet channel. This is shown in Figure 5.6.

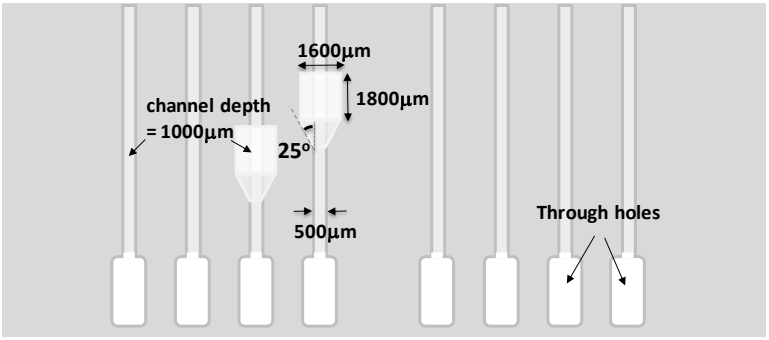

(a) Bottom layer of microfluidic channels

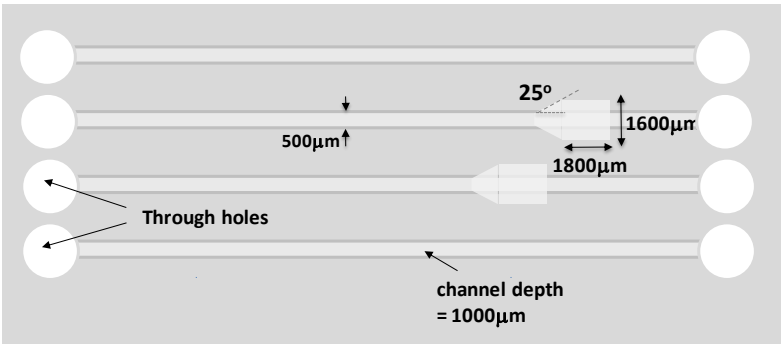

(b) Top layer of channels

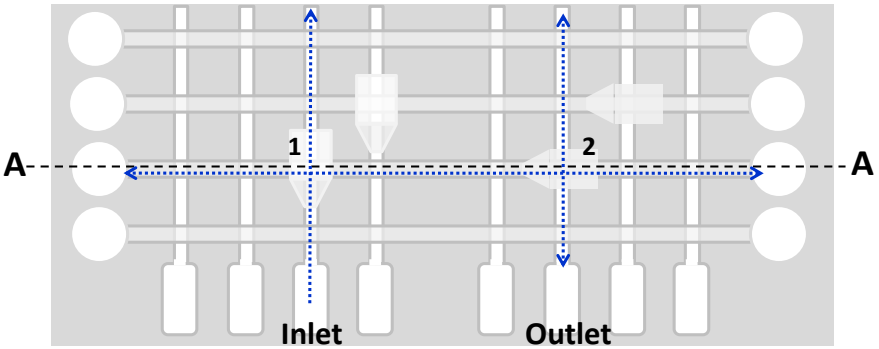

(c) Assembled device

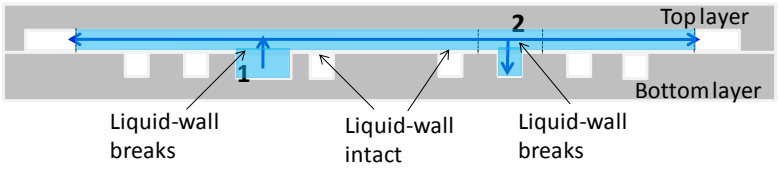

(d) Cross-sectional view across A-A, showing transfer of liquid

Figure 5.6: Schematic of passive transfer of liquid across microfluidic channels

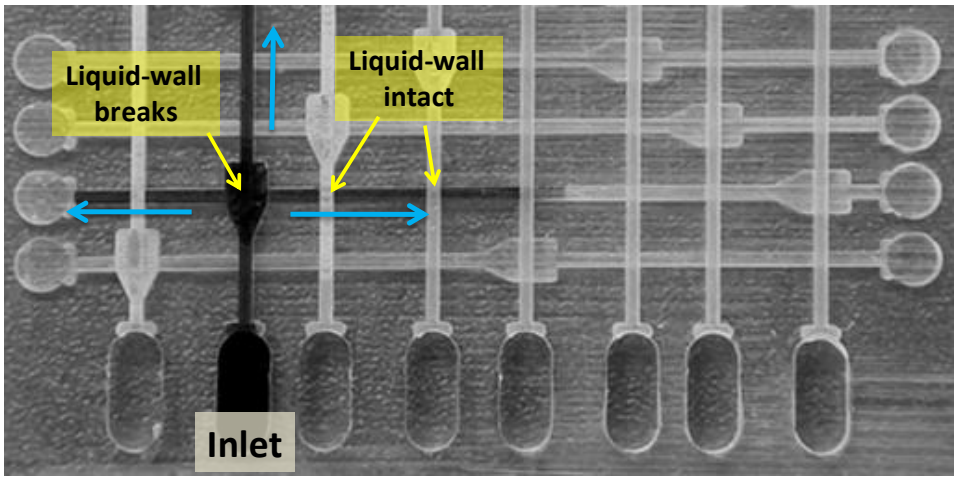

(a)

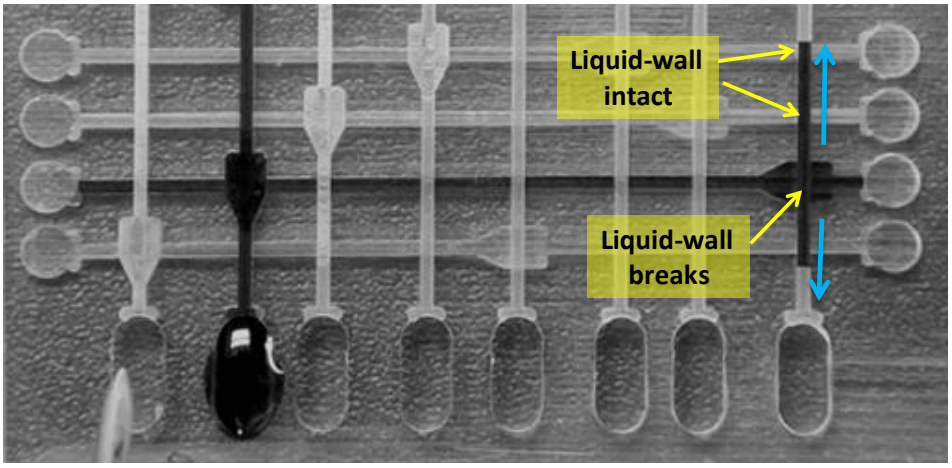

(b)

Figure 5.7: Controlled break of liquid-wall allows passive transfer of liquid across microfluidic channels

As can be seen from the cross-sectional view of the device, Figure 5.6b, junctions 1 and 2 allow controlled transfer of liquid from inlet channel to a given outlet channel across several other microfluidic channels. The microfluidic device is fabricated using dimensions in Figure 5.5 and its operation is shown in Figure 5.7.

However, the demonstrated ‘transfer channel’ scheme requires that a slight positive pressure is always maintained at the inlet to break the liquid-wall and transfer the liquid. But as the liquid fills the channels, the pressure at the inlet drop will go down. This problem can be solved by connecting all the channels to a liquid reservoir, with a fresh drop volume, at regular intervals. This is shown in Figure 5.8. As can be seen, the liquid from the new drop forms a liquid wall with each channel. When the channels carrying liquid come in contact with the liquid reservoir, through the liquid-wall, the pressure in the system increases for the next set of operations (due to the pressure being higher in the reservoir channel). Further, the reservoir liquid-wall is designed so as to keep it intact, as shown earlier.

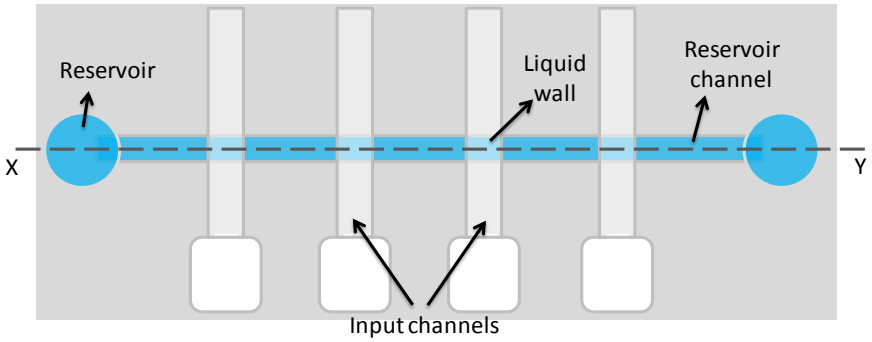

(a)

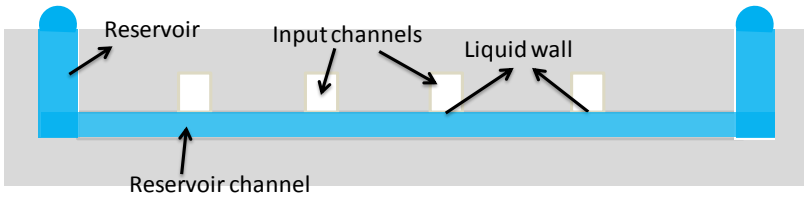

(b)

Figure 5.8: Reservoir channel is used to increase the inlet pressure downstream (a) Top view of reservoir channel forming liquid-wall with input channels (b) Section X-Y

5.5 Summary

Liquid-wall flow has been accomplished in a microfluidic device, without the use of surface patterning. The walls in the designed channel can be manipulated dynamically by simply introducing liquid into the adjacent channel, thus turning them 'off'. A theoretical model has been developed for predicting the break pressure of the liquid-wall. Further, geometrically manipulated breaking of liquid-wall has been used to control the transfer liquid into desired microfluidic channels in a multi-layered microfluidic device.

Also, given the significant liquid-gas interface area offered by liquid-walls, they could form artificial-lungs for chemical analysis [7]. Fabrication of such channels with intermittent side walls could make these systems practical by keeping the break pressure of the liquid-wall high with little compromise on the liquid-gas interface area. Pressure driven flow in such a system would be limited by the length of flow channel for a given flow rate.

Additional Information Available

Appendix B shows the calculations for the limit in height of the liquid-wall.

5.6 References

1. Zimmermann, M., Schmid, H., Hunziker, P., Delamarche, E., Lab on a Chip, 7, 119-125 , 2007.

2. Chung, K.H., Hong, J. W., Lee, D.S., Yoon, H.C., Analytica Chimica Acta, 585, 1-10, 2007
3. Feng, Y., Zhou, Z., Ye, X., Xiong, J., Sensors and Actuators A, 108, 138 – 143, 2003
4. Zhao, B., Moore, J. S., Beebe, D. J., Langmuir, 19, 1873-1879, 2003
5. Man, P. F., Mastrangelo C. H., Burns M. A. and Burke D. T., MEMS'98, pp 45–50, 1998
6. Madou, M.J., Kellogg, G.J., Proceedings of the SPIE, Vol. 3259, pp. 80–93, 1998
7. Zhao, B., Moore, J. S., Beebe, D. J., *Science, 291*, 1023-1026, 2001
8. R.M. Moroney, MSM' 98, Santa Clara, CA, 1998 pp. 526 ; J. Melin, N. Roxhed, G. Gimenez, P. Griss, W. Van der Wijngaart, G. Stemme, 12th International Conference on Transducers, Solid-State Sensors, Actuators and Microsystems 2 (2003) 1562.
9. Sung-Jin Kim, Yong Taik Lim, Haesik Yang,Yong Beom Shin, Kyuwon Kim, Dae-Sik Lee, Se Ho Park, Youn Tae Kim., Analytical Chemistry 77, no. 19 (2005) 6494
10. T. Young, G. Peacock, editor. Miscellaneous works, London' J. Murray, Vol. 1, 1855
11. Jun Zeng, Manish Deshpande, Ken B. Greiner, John R. Gilbert, ASME 2000.
12. Jerry M. Chen, Po-Chun Huang, Mou-Gee Lin, Microfluid Nanofluid 4 (2008) 427.
13. Jerry M. Chen, Chun-Yi Chen, Chia-Hung Liu, Jap. J. Applied Physics 47, no. 3, (2008) 1683.
14. Hansang Cho, Ho-Young Kimb, Ji Yoon Kang, Tae Song Kim, J. Colloid and Interface Science 306 (2007) 379.
15. E. Kim, G.M.J. Whitesides, Phys. Chem. B. 101 (1997) 855

APPENDIX A: Determination of trapped volume and modified Gibbs Energy Barriers

The geometry of the roughness profile physically limits the states accessible to the drop. This has been discussed in detail in the paper and here I present the calculations used to determine the trapped volume and the modified Gibbs energy barriers.

Consider Figure A.1, the two triangles show the roughness features and B1'-B1 and B2'-B2-C2 represent the tangents at the liquid-air interface, at the point of contact of liquid with the solid, for metastable state B1 and an intermediate state C2 respectively. A co-ordinate system is established with C1 as the origin. Further, as mentioned in the paper, it is assumed that the drop has a single radius of curvature at any given x.

It has been pointed out that C2 is a non-equilibrium state and therefore the results from the calculations should be interpreted only qualitatively.

A.1: Calculation of trapped volume

As the volume of the drop is constant,

Volume of drop at B1 = Volume of drop at C2 < A.1.1>

Where, Volume of drop at B1 = f (x, β, θ_1, Pitch) and Volume of drop at C2 = f (x, β, α, Pitch), and can be calculated as described in the paper.

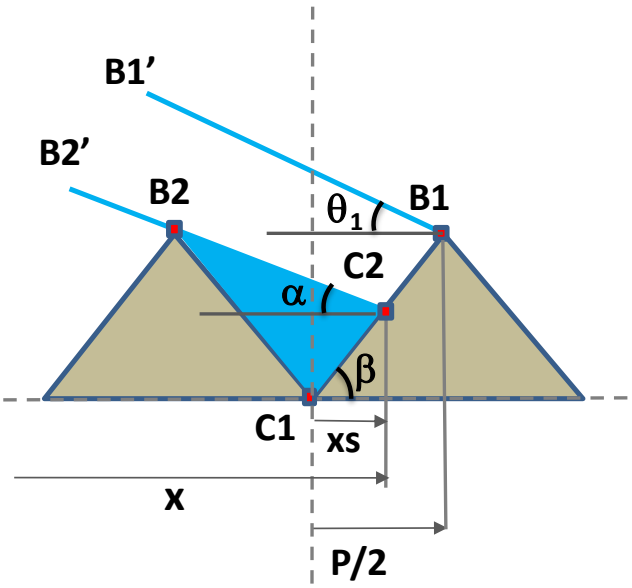

Figure A.1: Schematic of liquid-air interface for a 2D drop

Since B2 (-P/2, P/2*tanβ) and C2 (x_s, x_s*tanα) lie on line B2'-C2, equation for the line B2'-C2 is:

$$x_s \tan\beta = (x_s + P/2) * \tan\alpha + P/2 * \tan\beta \qquad \text{<A.1.2>}$$

The values of x_s and α can be found by solving simultaneous equations A.1.1 and A.1.2.

The trapped volume, Vsm given by the area of triangle B2-C1-C2 is calculated as:

$$Vsm = 2 * x_s * P/2 * \tan\beta \qquad \text{<A.1.3>}$$

A.2: Calculation of Gibbs energy for trapped volume

To calculate Gibbs energy of the trapped volume, it is assumed that when the drop moves to metastable state B2, the trapped volume attains minimum energy state by intersecting the sides of the roughness features at Young's contact angle. This is shown in Figure A.2. The curvature of the liquid-air interface for the trapped volume is neglected and the energy is given as:

$$GE\,\mathrm{Re}l._{TrappedVol} = \gamma_{LA}(-\cos\theta_Y * [\frac{2W}{\cos\beta}] + 2W) \qquad \text{<A.2.1>}$$

Where,

$$W = \sqrt{2 * Vsm / \tan\beta}$$

As stated earlier, γ_{LA} has been assumed to be 1 for this study.

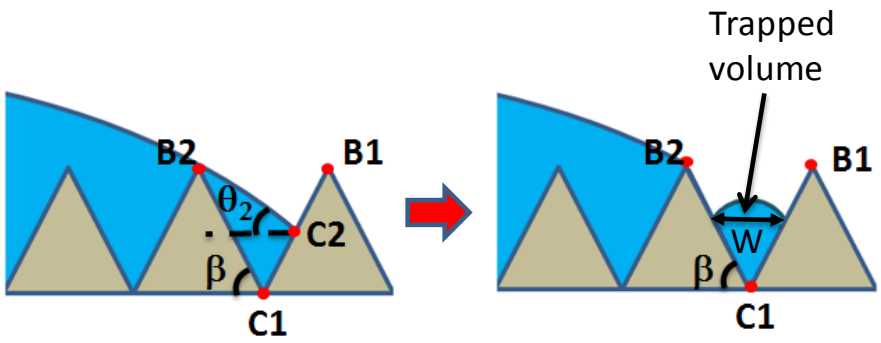

Figure A.2: Trapped volume

A.3: Calculation of modification in Gibbs energy barriers

The modified Gibbs energy barrier for metastable state B1 is given as:

$$GEB\text{-}L_{(B1)\,\mathbf{MOD}} = GE_{C2} - GE_{B1}$$

The relative Gibbs energy (GE) of the drop at point C2 and B1 can be determined by using equation 6, as x_s, α and θ_1 are known.

GEB-S for state B2 is similarly affected and can be calculated as:

$$GEB\text{-}S_{(B2)\,\mathbf{MOD}} = GE_{B2} - GE_{C2}.$$

To determine the relative GE at point B2, Vsm is subtracted from the drop volume and thereafter equation 6 is used along with volumetric constraint for calculations. The energy of the trapped volume is also included in the total energy of the system.

APPENDIX B: Maximum height and radius of curvature for liquid-wall flow

The maximum depth of the flow channel is determined by the weight of liquid that the liquid-meniscus can sustain. The same can be calculated by using Young's equation –

$$\Delta P = -\gamma(\frac{1}{R1} + \frac{1}{R2}) \qquad \text{<B.1>}$$

Where R1 and R2 are the radii of curvature of the liquid-wall. Assuming R2>> R1, implying length of liquid-wall is much greater than its height -

$$\Delta P = -\gamma(\frac{1}{R1}) = \rho g(W - Y); L >> W \qquad \text{<B.2>}$$

Noting from geometry that 1/R1 = dθ/dS, where S is the length of the meniscus and non-dimensionalizing the equation using capillary length - l_o = sqrt(γ/ρg),

$$-\frac{d\theta}{ds} = (w - y) \qquad \text{<B.3>}$$

In the above equation, the lower case subscripts - s, r2, w and y represent non-dimensionalized S, R2, W and Y respectively. Equation B.3 has been solved by Saif et al. [Saif, T., J. Fluid Mech., 473 (2002) 321]. Using the same method, it can be shown that –

$$\frac{w^2}{2} = -(\cos\phi - \sin\theta_0) \qquad \text{<B.4>}$$

Or,

$$W = \sqrt{\frac{\gamma}{\rho g}}\sqrt{2(\sin\theta_0 - \cos\phi)} \qquad \text{<B.5>}$$

For water, the maximum height turns out to be ~3.8mm for a contact angle of 90^o (considering only hydrophilic substrates)

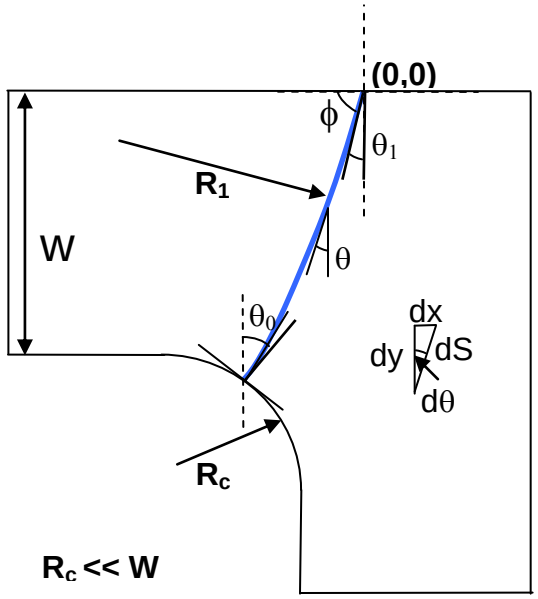

Figure B.1: Schematic of liquid meniscus forming the liquid-wall

Similarly, the maximum radius of curvature that the liquid-flow can make is restricted by the break pressure of the liquid-wall. As the liquid-flow turns, the radius of curvature on the inside of the turn is of opposite sign to the one made by liquid meniscus/liquid-wall. Thus, the liquid-wall can break in such a situation. The max. radius of curvature can be calculated by equating the break pressure to zero –

$$\Delta P_{break} = 0 = -\gamma(\frac{1}{R1} + \frac{1}{R2}) - \rho g * W \quad \text{<B.6>}$$

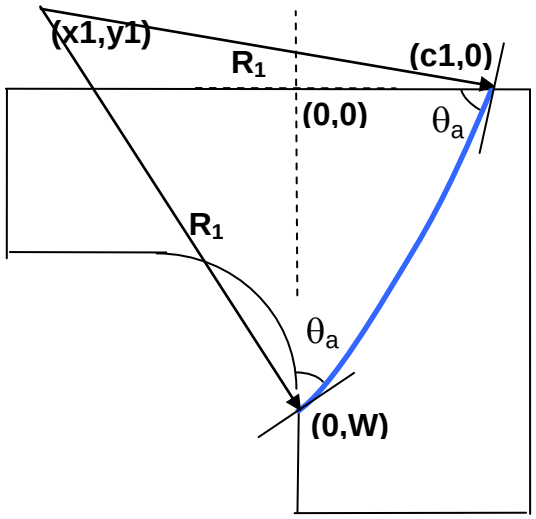

Figure B.2: Co-ordinate system set-up for radius of curvature calculation

Neglecting the contribution due to the weight of liquid, R2, max = |R1|. R1 can be calculated by solving the following simultaneous equations (Figure B.2) –

$$y1 = x1 * \tan\theta_a + W \quad \text{<B.7>}$$

$$y1 = (x1 - c1) * \tan(90 - \theta_a) \quad \text{<B.8>}$$

$$R1 = \sqrt{x1^2 + (y1 - W)^2} \quad \text{<B.9>}$$

$$R1 = \sqrt{(x1 - c1)^2 + y^2} \quad \text{<B.10>}$$

Height of liquid-wall (microns)	Max. radius of curvature (microns)
100	141
200	283
500	707

Table B.1: Max. radius of curvature for liquid-wall flow

Author's Biography

Tarun Malik was born on March 25th, 1981 in New Delhi, India. He received his B.E. degree in Mechanical Engineering from Delhi College of Engineering, Delhi, India in 2002. Tarun then joined Department of Mechanical Engineering at University of Illinois, Urbana-Champaign in August 2004 to pursue M.S. He worked with Prof. Clark Bullard on his Master's thesis: 'Exploring component design and system tradeoff' and was part of the Air Conditioning and Refrigeration Center (ACRC). Thereafter, he joined Behr America, an automotive air-conditioning company based in Troy, MI in August, 2004. After two years of experience, he decided to pursue PhD and returned to University of Illinois in August 2006. He joined Prof. Nicholas X. Fang's group in January 2007. His research has been focused on understanding solid-liquid interfacial phenomena and developing applications based on the same. After receiving his Ph.D., Tarun will join Intel Corporation in Portland, Oregon.